Performance-limiting nanoscale trap clusters at grain junctions in halide perovskites

https://doi.org/10.1038/s41586-020-2184-1

Received: 5 December 2018

Accepted: 17 February 2020

Published online: 15 April 2020

Check for updates

Tiarnan A. S. Doherty[1,9], Andrew J. Winchester[2,9], Stuart Macpherson[1], Duncan N. Johnstone[3], Vivek Pareek[2], Elizabeth M. Tennyson[1], Sofiia Kosar[2], Felix U. Kosasih[3], Miguel Anaya[1], Mojtaba Abdi-Jalebi[1,7], Zahra Andaji-Garmaroudi[1], E Laine Wong[2], Julien Madéo[2], Yu-Hsien Chiang[1], Ji-Sang Park[4,8], Young-Kwang Jung[5], Christopher E. Petoukhoff[2], Giorgio Divitini[3], Michael K. L. Man[2], Caterina Ducati[3], Aron Walsh[4,5], Paul A. Midgley[3], Keshav M. Dani[2]✉ & Samuel D. Stranks[1,6]✉

Halide perovskite materials have promising performance characteristics for low-cost optoelectronic applications. Photovoltaic devices fabricated from perovskite absorbers have reached power conversion efficiencies above 25 per cent in single-junction devices and 28 per cent in tandem devices[1,2]. This strong performance (albeit below the practical limits of about 30 per cent and 35 per cent, respectively[3]) is surprising in thin films processed from solution at low-temperature, a method that generally produces abundant crystalline defects[4]. Although point defects often induce only shallow electronic states in the perovskite bandgap that do not affect performance[5], perovskite devices still have many states deep within the bandgap that trap charge carriers and cause them to recombine non-radiatively. These deep trap states thus induce local variations in photoluminescence and limit the device performance[6]. The origin and distribution of these trap states are unknown, but they have been associated with light-induced halide segregation in mixed-halide perovskite compositions[7] and with local strain[8], both of which make devices less stable[9]. Here we use photoemission electron microscopy to image the trap distribution in state-of-the-art halide perovskite films. Instead of a relatively uniform distribution within regions of poor photoluminescence efficiency, we observe discrete, nanoscale trap clusters. By correlating microscopy measurements with scanning electron analytical techniques, we find that these trap clusters appear at the interfaces between crystallographically and compositionally distinct entities. Finally, by generating time-resolved photoemission sequences of the photo-excited carrier trapping process[10,11], we reveal a hole-trapping character with the kinetics limited by diffusion of holes to the local trap clusters. Our approach shows that managing structure and composition on the nanoscale will be essential for optimal performance of halide perovskite devices.

Visualizing the nanoscale trap clusters

We solution-processed 'triple-cation' lead halide $(Cs_{0.05}FA_{0.78}MA_{0.17})Pb(I_{0.83}Br_{0.17})_3$ (FA, formamidinium; MA, methylammonium) perovskite films (bandgap of ~1.62 eV; Extended Data Fig. 1) on indium-tin-oxide-(ITO-)coated glass or electron-transparent SiN substrates, representative of materials used in high-efficiency solar cells[12] (see Methods; characterization of films and devices shown in Extended Data Fig. 2). Uniquely shaped gold particles were deposited on top of the films to act as fiducial markers for the correlative experiments[8] (see Methods). In our experimental set-up for photoemission electron microscopy (PEEM) (Fig. 1a, inset), we first measured spatially averaged

[1]Cavendish Laboratory, University of Cambridge, Cambridge, UK. [2]Femtosecond Spectroscopy Unit, Okinawa Institute of Science and Technology Graduate University, Onna-son, Japan. [3]Department of Materials Science and Metallurgy, University of Cambridge, Cambridge, UK. [4]Department of Materials, Imperial College London, London, UK. [5]Department of Materials Science and Engineering, Yonsei University, Seoul, South Korea. [6]Department of Chemical Engineering and Biotechnology, University of Cambridge, Cambridge, UK. [7]Present address: Institute for Materials Discovery, University College London, London, UK. [8]Present address: Department of Physics, Kyungpook National University, Daegu, South Korea. [9]These authors contributed equally: Tiarnan A. S. Doherty, Andrew J. Winchester. ✉e-mail: kmdani@oist.jp; sds65@cam.ac.uk

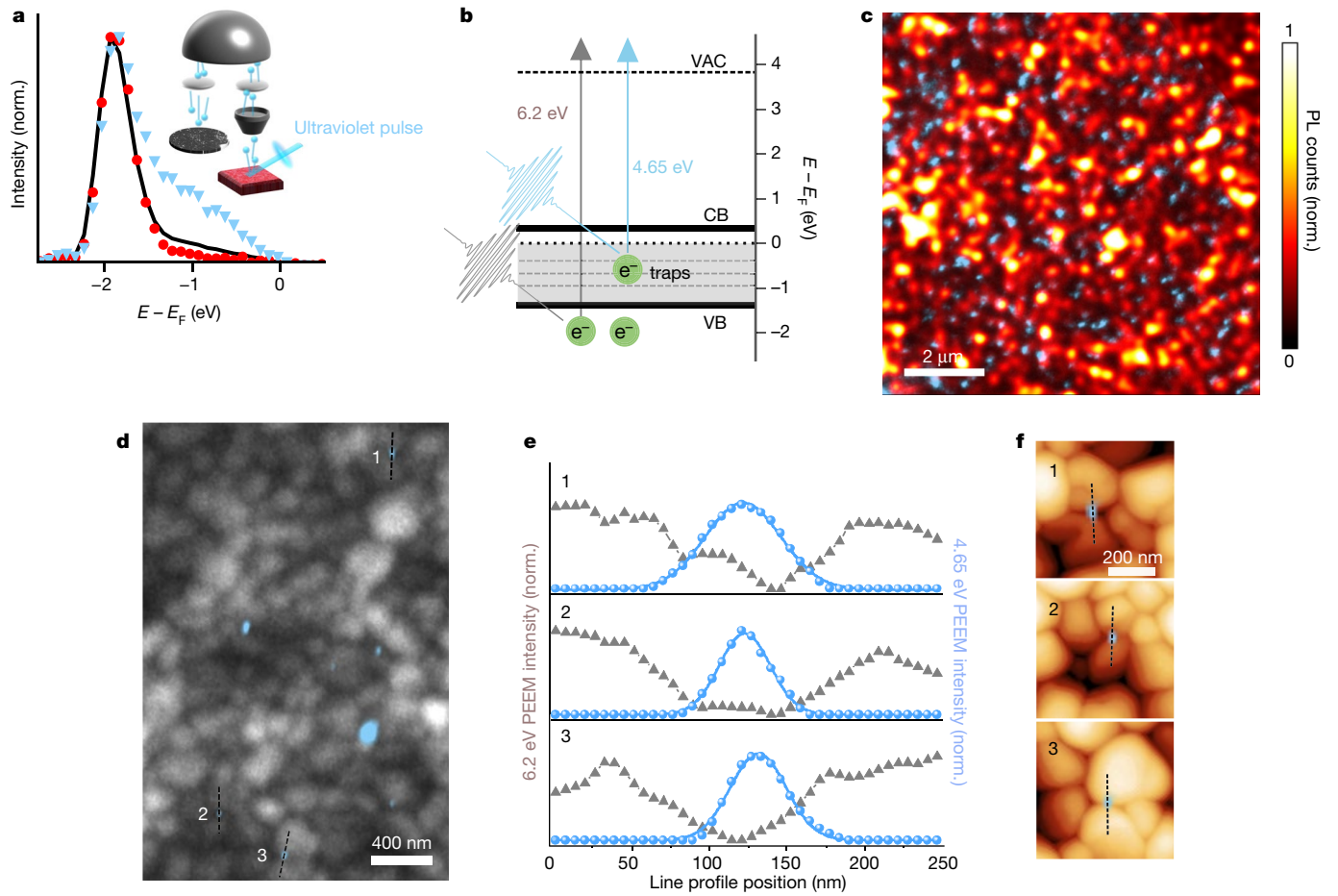

Fig. 1 | Photoemission electron microscopy revealing the spatial distribution of trap sites leading to non-radiative power losses. Results are for $(Cs_{0.05}FA_{0.78}MA_{0.17})Pb(I_{0.83}Br_{0.17})_3$ films. **a**, Spatially averaged photoemission spectra from a scan area ~10 µm × 10 µm (solid black line), and spatially resolved spectra from (blue triangles) and away from (red circles) a trap cluster. Inset, schematic of PEEM set-up for imaging photoelectrons (blue spheres; lines indicate direction of motion) emitted by the UV laser pulse (blue beam). Collected photoelectrons are imaged and magnified with electromagnetic lenses (grey cone and ovals) and can be energy-filtered (silver hemisphere) before forming the final image. **b**, Energy-level diagram of the perovskite sample referenced to the Fermi level at 0 eV. Arrows represent transitions between states in the valence band (VB), conduction band (CB), trap states, and vacuum (Vac) for the UV laser pulses (4.65-eV and 6.2-eV photons, blue and grey arrows, respectively). The CB position is estimated from the bandgap of the sample (~1.62 eV; see Extended Data Fig. 1) relative to the band edge measured from **a**. **c**, Anticorrelation between nanoscale trap clusters mapped by PEEM (blue) and local PL intensity . **d**, PEEM image from 4.65-eV pulses showing the location of nanoscale trap clusters (blue) overlaid on the 6.2-eV pulse PEEM image from the entire film, generated by photoemission from the valence band, showing the grain morphology (grey). **e**, Line profile of the intensity from the 4.65-eV pulse (blue) against the intensity from the 6.2-eV pulse (grey). Numbering corresponds to regions of interest in **d**. **f**, The same regions of interest as in **d** and **e**, with PEEM maps from the 4.65-eV probe overlaid on AFM images.

photoemission spectra using an ultraviolet (UV) pulse energy of 6.2 eV. We took care to minimize the total UV exposure during our experiments, such that we see negligible changes in the perovskite properties as a result of these measurements (see Methods and Extended Data Figs. 3 and 4).

In spatially averaged spectra (black line in Fig. 1a) taken from an area of the sample ~10 µm × 10 µm, we observe an occupied density of states extending into the bandgap, from above the valence band at around −1.9 eV up to the Fermi level. Consistent with previous macroscopic photoemission measurements on thin-film[13] $MAPbI_3$ and cleaved single crystal[14] $MAPbBr_3$, we attribute these to subgap trap states—that is, states lying within the bandgap that trap charge carriers.

A schematic of the different energy levels with the main optical transitions of the UV pulses is shown in Fig. 1b. The 6.2-eV pulse energy is just sufficient to photoemit electrons from the valence-band edge (grey arrow, Fig. 1b). The absorption depth of the UV pulses (<10 nm) dictates the depth into the sample that we probe, as the mean free path for the inelastic photo-emitted electrons with energy of a few electronvolts will be larger than 10 nm (refs. [15,16]). Hence, these detected trap states are located near the surface of the film (<10 nm), where trap densities are expected to be high and detrimentally impact the device performance[17].

To understand the distribution of these occupied subgap trap states, we spatially resolve the photoemitted electrons. For this, we use 4.65-eV UV pulses, which provide enough energy to overcome the work function (~3.9 eV) but not enough to photoemit electrons from the valence states, as illustrated by the blue arrow in Fig. 1b. This allows us to selectively image the subgap states without needing to energy-resolve the photoelectrons. These photoemitted electrons are imaged in the microscope by electromagnetic lenses (inset of Fig. 1a) to achieve a spatial resolution of 20 nm. Strikingly, as shown in the blue regions representing the PEEM intensity from subgap trap states in Fig. 1c, we observe many isolated nanoscale trap sites on the sample, ranging in size from a few tens to a few hundreds of nanometres (see Extended Data Fig. 5 for distributions). Spatially resolved photoemission spectra from these sites show a large density of subgap states (blue triangles, Fig. 1a), but in spectra taken at regions away from these sites, the subgap states are notably absent (red circles, Fig. 1a). We observe the

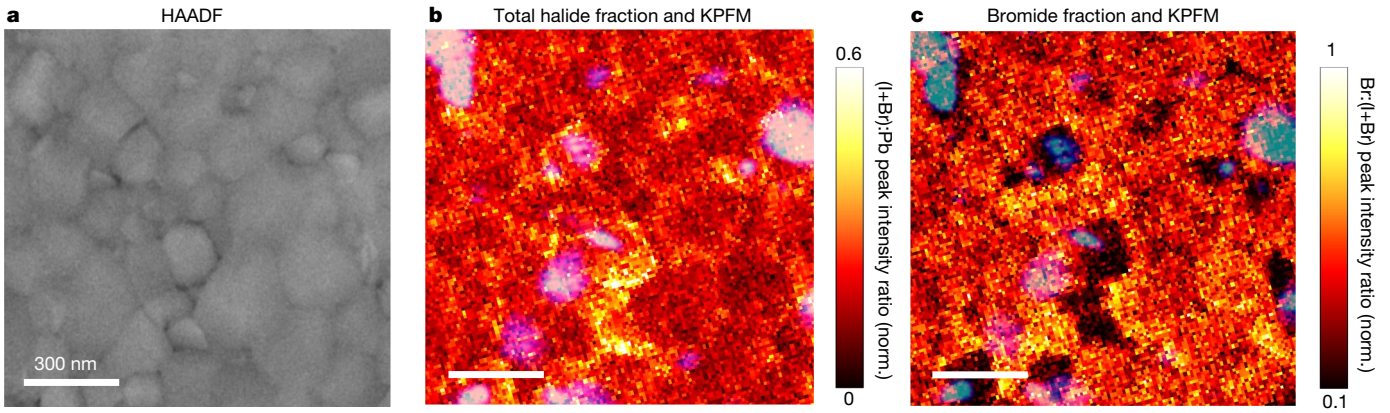

Fig. 2 | Probing the composition of grains associated with nanoscale trap clusters. Results are for $(Cs_{0.05}FA_{0.78}MA_{0.17})Pb(I_{0.83}Br_{0.17})_3$ thin films. **a**, HAADF-STEM image of a region of interest, revealing morphological grains. **b**, Ratio of total halide intensity counts relative to Pb intensity, $(I(I\,L\alpha) + I(Br\,K\alpha))/I(Pb\,L\alpha)$, ascertained from STEM-EDX measurements. Some grains, and their grain boundaries, are particularly halide-rich. **c**, Fraction of bromide intensity counts out of total halide counts, $I(Br\,K\alpha)/(I(I\,L\alpha) + I(Br\,K\alpha))$. The same distinct grains that were rich in halide are bromide-poor, whereas the rest of the region of interest (bulk parent material) shows a homogenous distribution of Br. The compositional data in both **b** and **c** are normalized to between 0 and 1 by subtracting the minimum value and scaling with the maximum value from the respective map of intensity ratio for the peaks. The trap clusters, indicated by KPFM measurements (blue), are overlaid on **b** and **c** and appear at the junction between the stoichiometrically 'inhomogeneous' grains and the bulk parent material.

same behaviour from energy-resolved images using the 6.2-eV pulses (Extended Data Fig. 6).

In Fig. 1c, we show a confocal photoluminescence (PL) map of a region of the sample, highlighting the substantial spatial heterogeneity in the luminescence intensity, and overlay this on a PEEM image of the trap sites at the same location. We find a strong anticorrelation between the spatial location of these trap sites (that is, PEEM intensity) and local PL intensity: regions of high PL intensity have very few trap sites, whereas regions with a high density of trap sites correspond to low PL intensity. A pixel-by-pixel plot of PL against PEEM intensity in Extended Data Fig. 7 further elucidates the role played by the trap sites in contributing to non-radiative losses. The surface traps we observe here in PEEM have a large impact on the observed PL variation because even photo-excited carriers generated deeper in the bulk can diffuse much of the ~500-nm thickness of the film to the surface[18]. Bulk traps may additionally influence the PL, but these are likely to be of lower density. We do not observe any strong subgap absorption in our films (Extended Data Fig. 1). Furthermore, Kelvin probe force microscopy (KPFM) measurements overlaid on PEEM trap images reveal that the trap-rich local clusters observed in PEEM have a lower contact potential difference (CPD) with respect to the surrounding regions; a linear relationship between the CPD and the PEEM trap intensity allows us to use PEEM and KPFM measurements together as independent spatial indicators of the local trap distribution (Extended Data Fig. 7). These results reveal that micrometre-scale dark regions in PL contain discrete nanoscale high-density clusters of traps, rather than one single, uniformly defective region. The strong relationship between these trap clusters and the PL and CPD properties demonstrates the substantial impact of these trap clusters on optoelectronic performance.

In Fig. 1d, we overlay these nanoscale trap clusters (blue, 4.65-eV pulses) on the grain morphology of the film ascertained from valence-band photoemission (grey, 6.2-eV pulse), which shows morphological grain boundaries at sites where the photoemission intensity is lowered. This overlay reveals that the nanoscale trap clusters are located primarily at the junction between morphological grains: line profiles of PEEM intensity from the traps (blue) and morphological grain structure (grey) in Fig. 1e show that the trap clusters occur at specific grain boundaries. Complementary atomic force microscopy (AFM) images on the same scan regions and PEEM sites show that these regions are indeed morphological grain boundaries (Fig. 1f).

Local properties at defective junctions

To probe how the nanoscale trap clusters, identified by PEEM and KPFM, relate to composition, we performed high-angle annular dark-field scanning transmission electron microscopy (HAADF-STEM), energy-dispersive X-ray spectroscopy (STEM-EDX) and KPFM measurements on the same scan area of a $(Cs_{0.05}FA_{0.78}MA_{0.17})Pb(I_{0.83}Br_{0.17})_3$ sample. In Fig. 2a, we show a HAADF-STEM image revealing morphological grain structure within the correlated region of the film. In Fig. 2b, we show the normalized ratio of total halide-to-lead peak intensity (I), $(I(I\,L\alpha) + I(Br\,K\alpha))/I(Pb\,L\alpha)$, obtained from STEM-EDX maps with a spatial resolution of ~10 nm. This image reveals that some distinct morphological grains contain an excess of halide relative to the rest of the region of interest, which is particularly exaggerated at the grain boundaries. We show in Fig. 2c that these same morphological grains are also poor in bromide (with respect to the surrounding material), ascertained from the normalized bromide fraction of peak intensity out of total halide counts, $I(Br\,K\alpha)/(I(I\,L\alpha) + I(Br\,K\alpha))$. This is consistent with these grains appearing brighter in the HAADF-STEM image (Fig. 2a) because there are fewer light atoms (Br) and more heavy atoms (I) in these grains. The observed relative variation in halide content is not related to variations in the Pb content across the scanned region (Extended Data Fig. 8). When we overlay the trap regions determined from KPFM measurements (blue regions) on the compositional intensity maps in Fig. 2b and c, we find that the nanoscale trap clusters are almost exclusively associated with interfaces between these compositionally inhomogeneous morphological grains and the more homogeneous surrounding material. We refer to these regions herein as stoichiometrically 'inhomogeneous grains' and the surrounding film as 'bulk parent material'. These results reveal that most trap clusters appear at heterojunctions between these sites.

To better understand the local crystallography of these inhomogeneous grains and their relationship with trap clusters at grain boundaries, we correlate PEEM measurements with low-dose scanning electron diffraction (SED) microscopy and STEM-EDX measurements. To avoid beam-induced damage under electron radiation while maintaining a spatial resolution of ~4 nm, our SED experiments were performed with a local electron dose of ~6 e $Å^{-2}$ (see Methods for experimental parameters to calculate dose), substantially lower than reported dose limits for halide perovskites in crystallography

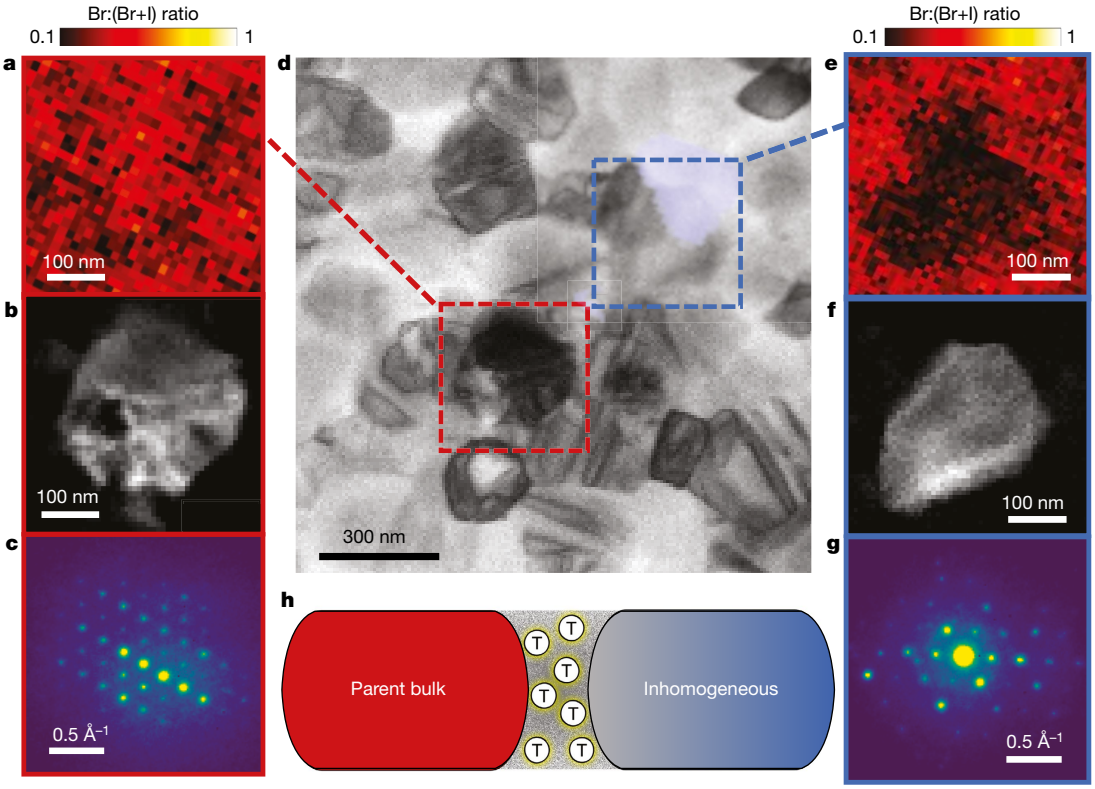

Fig. 3 | High-resolution diffraction and compositional properties of nanoscale trap-rich heterojunctions. Results are for $(Cs_{0.05}FA_{0.78}MA_{0.17})Pb(I_{0.83}Br_{0.17})_3$ films. A virtual bright-field image shown in **d** is extracted from SED measurements and overlaid on a PEEM map showing the deep trap clusters (blue) on the same scan region. A pristine region (red box) and inhomogeneous region (blue box) are subsequently analysed. **a**, Ratio $I(\mathrm{Br\,K\alpha})/(I(\mathrm{I\,L\alpha})+I(\mathrm{Br\,K\alpha}))$ extracted from a STEM-EDX map of the pristine parent region away from a trap site showing a homogeneous halide ratio. **b**, Image of a pristine grain extracted from the SED data from the red region of interest in **d**. **c**, Mean diffraction pattern of the compositionally homogenous grain in **a** and **b**, revealing a cubic crystal structure corresponding to the nominal pristine composition. **e**, Ratio $I(\mathrm{Br\,K\alpha})/(I(\mathrm{I\,L\alpha})+I(\mathrm{Br\,K\alpha}))$ extracted from a STEM-EDX map of the blue region of interest in **d**, revealing the presence of an inhomogeneous grain. **f**, Image of a grain extracted from SED data from the blue region of interest in **d**. **g**, Mean diffraction pattern of an inhomogeneous grain from **e** and **f**, which cannot be directly indexed to a cubic $FAPb(I_{0.83}Br_{0.17})_3$ model. **h**, Schematic showing that the traps (T) accumulate at the interface between compositionally and structurally homogeneous cubic parent regions and the inhomogeneous, distorted regions. Compositional data in both **a** and **e** are normalized to between 0 and 1 by subtracting the minimum value and scaling with the maximum value from the respective map of peak intensity ratio.

studies of ~100 e Å^{-2} (ref. [19]). We show a virtual bright-field image of a region of a thin-film sample of $(Cs_{0.05}FA_{0.78}MA_{0.17})Pb(I_{0.83}Br_{0.17})_3$ in Fig. 3d, which we obtain by integrating the SED intensity around the direct beam as a function of probe position, and overlay on this image the PEEM measurement from the same scan area showing the location of the traps (blue). In Fig. 3a, we show a STEM-EDX map of the selected area from the bulk parent material in Fig. 3d that is not associated with a trap cluster and has a uniform halide composition. Within this region, we identify a pristine grain (Fig. 3b) from the parent material by performing a non-negative matrix factorization (NMF) analysis of the SED data. The grain revealed by NMF has the mean diffraction pattern shown in Fig. 3c and can be indexed to near the [111] zone axis of cubic $FAPb(I_{0.83}Br_{0.17})_3$ (see Extended Data Fig. 8 for indexation). We observe a similar cubic structure across other regions of the sample with homogeneous composition. A representative compositionally inhomogeneous grain (blue box in Fig. 3d) is shown by the normalized halide intensity ratio from the STEM-EDX map (Fig. 3e) and corresponds to a grain identified by NMF (Fig. 3f). This grain is directly associated with the nanoscale trap cluster at its interface with an adjacent pristine grain (blue PEEM spot visualized in Fig. 3d overlay). The mean diffraction pattern associated with the inhomogeneous grain is shown in Fig. 3g and is structurally distinct from the pristine material. This structure cannot be directly indexed to a cubic $FAPb(I_{0.83}Br_{0.17})_3$ or other known perovskite or PbI_2 model (see Methods for further discussion).

Ultra-fast hole trapping

Having imaged and analysed localized nanoscale trap sites on the film surface, we now study the specific influence of these traps on photo-excited charge-carrier recombination by using time-resolved PEEM (TR-PEEM) measurements to visualize the ultrafast trapping dynamics[10,11]. We first photoexcite the sample with a near-infrared, ultrafast pump pulse (1.55 eV) and then image it with a time-delayed ultrafast UV probe pulse (Fig. 4b). Here, we study the dynamics of an iodide-only analogue sample $(Cs_{0.05}FA_{0.78}MA_{0.17})PbI_3$, which has a bandgap of ~1.54 eV (Extended Data Fig. 1), thus enabling a resonant excitation condition. We see similar trap characteristics to those in the bromide-containing samples (Extended Data Figs. 5, 6) and also see similar kinetics (Extended Data Fig. 9). We use the 4.65-eV UV probe pulses to image electrons exclusively from occupied trap states (blue transition in Fig. 1b). Thereby, we are able to construct movies of the photocarrier trapping dynamics from sequences of images at varying pump-probe time delays (see Supplementary Videos 1 and 2).

On photoexcitation, we first observe that the photoemission intensity measured from the trap states decreases (Fig. 4c), implying a decrease in electron occupation after photoexcitation—that is, trapping of photo-excited holes (Fig. 4c inset). The absence of a sharp decrease in the photoemission signal at zero time delay indicates that there is no detectable direct excitation of electrons out of the trap states by the pump. We then compare the TR-PEEM movies between low- and

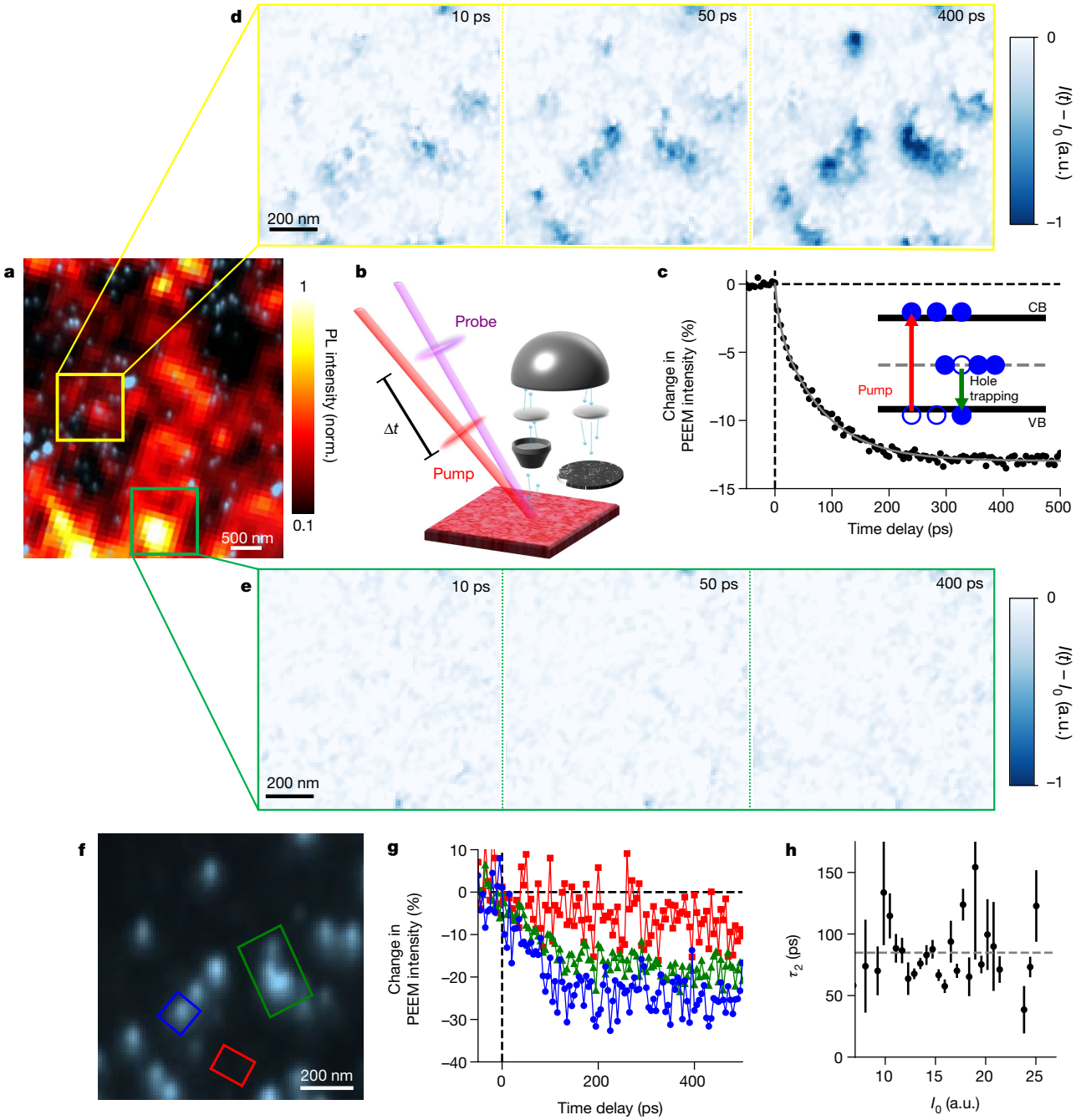

Fig. 4 | Nanoscale photo-excited carrier trapping dynamics. a, Overlaid PL and PEEM images from $(Cs_{0.05}FA_{0.78}MA_{0.17})PbI_3$ thin film. **b**, Schematic of the TR-PEEM set-up for time-resolved imaging of photoelectrons. A pump pulse (1.55 eV, red beam) first excites the sample. A time-delayed (Δt) UV probe pulse (4.65 eV, violet) then measures the pump-induced change in electron population by photoemitting electrons (blue spheres) into the PEEM microscope. **c**, Measured TR-PEEM signal as a function of delay time, $I(t)$, plotted as the percentage change $(100 \times (I(t) - I_0)/I_0)$ in PEEM intensity against the initial non-photoexcited PEEM signal I_0 before arrival of the pump pulse (negative time delay). The signal is extracted from all the trap clusters within the field of view (~10 μm × 10 μm). The grey line is a double-exponential fit to the data with time constants $\tau_1 = 7 \pm 2$ ps and $\tau_2 = 79 \pm 3$ ps, and amplitudes $A_1 = 2.4 \pm 0.4$ and $A_2 = 10.5 \pm 0.3$, where the error is the standard error from the fitting. Inset, a simplified energy diagram, where the pump photons (red arrow) excite electrons (blue circles) from the valence band to the conduction band. The trap states occupied by electrons can then trap holes (hollow blue circles), where an electron moves from the trap state to the valence band (green arrow). **d**, **e**, TR-PEEM images from the marked areas in **a**, showing the change in photoemission intensity ($I(t) - I_0$) with time delay after excitation. **f**, PEEM image of several traps (same location as **d**), with two trap clusters and a trap-free region marked (blue, green and red rectangles, respectively). **g**, Extracted TR-PEEM signal from the nanoscale spots marked in **f**. The two marked trap clusters (blue circles and green triangles) show the hole-trapping dynamics, whereas the trap-free area (red squares) shows a negligible signal change. **h**, Fitted time constants τ_2 for different trap-site intensities I_0. Error bars denote the standard error from the exponential fitting for each intensity bin, where the number of traps measured for each bin is shown by the histogram in Extended Data Fig. 12b. The dashed grey line represents the mean (85 ps) of the data.

high-PL regions of the sample (Fig. 4a). In regions of low PL efficiency (yellow box in Fig. 4a), we see complex spatio-temporal dynamics with photo-excited holes being trapped at several discrete sites (Fig. 4d and Supplementary Video 1). In contrast, regions of high PL efficiency (green box in Fig. 4a) show little to no photo-excited hole trapping (Fig. 4e and Supplementary Video 2). From the time-resolved

images (Fig. 4d and Supplementary Video 1), we extract spatially resolved dynamics from selected trap clusters. For local spots of substantial trap density (Fig. 4f, blue and green rectangles) we measure the photo-excited hole-trapping signal (Fig. 4g, blue circles and green triangles, respectively), whereas in regions of low trap density (Fig. 4f, red rectangle) we see no change in PEEM intensity (Fig. 4g, red squares). We observe this trend across different samples, different locations and for repeated measurements (see Extended Data Fig. 10 for additional TR-PEEM images). Previous reports on $MAPbI_3$ films have identified electron trapping as the dominant non-radiative pathway, with hole traps, if present, playing a lesser role[20,21]. By contrast, we show in these mixed-cation systems that hole traps influence charge-carrier dynamics on a subnanosecond timescale and directly correlate with the primary sites of non-radiative losses. Our measurements cannot exclude the additional possibility of electron traps in these mixed-cation films, particularly if the electron capture happens on a longer timescale.

We develop further insight into the hole-trapping dynamics through quantitative analysis of the process at different sites. First, a double-exponential fit to the spatially averaged data in Fig. 4c (see Methods for details and alternative equivalent approaches) is used to extract the trapping time, where the slower τ_2 time constant of 81 ± 21 ps is found to be the main contribution to the signal amplitude. We then extract the τ_2 time constant as a function of the trap density (proportional to the photoemission intensity I_0) from all the individual trap sites within the PEEM image, using a binning procedure (see Methods). We find that this dominant time component is independent of trap density (Fig. 4h), revealing that the initial trapping kinetics are not limited by the trap density of a site. Rather, we attribute this timescale of ~80 ps to the time it takes for photo-excited holes to reach the trap sites through diffusion. Assuming a diffusion coefficient D of ~1 $cm^2 s^{-1}$ (for intra-grain diffusion[22]), this timescale would correspond to a trapping length ($L = \sqrt{D\tau}$) of approximately 90 nm, which is comparable to half the mean distance between neighbouring trap sites for the samples (Extended Data Fig. 5). Such a diffusion-limited trapping process is consistent with previous diffraction-limited optical measurements[22].

Because of the resonant photoexcitation conditions in the time-resolved measurements reported here, we expect that thermal effects such as carrier heating or phonon bottlenecks[23] do not influence the dynamics we see and are not responsible for the removal of electrons from the occupied traps. However, other processes, such as carrier–carrier and carrier–phonon interactions or phonon-assisted trapping and de-trapping processes[24], may play a role. Under our experimental conditions, we are not able to observe a transient signal related to free carriers in the conduction band (see Methods for discussion), and therefore future work will require complementary measurements of carrier kinetics for a complete understanding of carrier recombination processes.

Discussion

Our combined results show that deep photo-excited hole traps form at the interfaces between pristine grains with expected halide ratios and cubic structure, and grains that are compositionally inhomogeneous with a distorted structure. Any heterogeneity in the local A-site cation distribution[25] could further exacerbate these defective junctions. The interface between the pristine material and compositionally inhomogeneous regions results in a distribution of electronic states above the valence band, which can be explained by a defect segregation that varies across the interface, for example, driven by the strain between the inhomogeneous phase and the parent material (see Fig. 3h). For iodine interstitial defects, which form charge transition levels deep in the bandgap that could trap holes[26–28], a higher concentration will be formed at the grain boundaries owing to the local excess of halide there[29]. Further work will be required to explain why deep trap states form at only one localized interface between the compositionally inhomogeneous grains and the bulk pristine material, although it may relate to grain orientation, or a specific strained contact point at which defects pool.

Our conclusions have implications for understanding the nanoscale behaviour of halide perovskites. We have shown that trap sites associated with non-radiative recombination—which influences charge-carrier lifetime and solar cell open-circuit voltage, and ultimately limits device performance[30]—appear in nanoscale clusters. Although there is consensus that device performance improves with better homogenization of the halide content in mixed-halide systems[31], the underpinning mechanism of this improvement has been unclear. The fact that these surface traps almost exclusively form at local junctions between grains provides rational strategies for the removal of harmful trap states, and suggests that further traps may not form at other locations. Thus, passivation and growth strategies that target the removal of these inhomogeneous and distorted grains will be critical for the elimination of performance losses and instabilities. The localized but sparsely distributed nature of the trap clusters may also give insight into the apparent defect tolerance of the materials. Finally, the correlated multimodal framework presented here has applications extending far beyond halide perovskites: the ability to locate and identify the structural and compositional origins of deep trap states will be applicable to a wide range of beam-sensitive semiconductor material families, including bulk inorganic and two-dimensional (2D) materials.

Online content

Any methods, additional references, Nature Research reporting summaries, source data, extended data, supplementary information, acknowledgements, peer review information; details of author contributions and competing interests; and statements of data and code availability are available at https://doi.org/10.1038/s41586-020-2184-1.

1. Jiang, Q. et al. Surface passivation of perovskite film for efficient solar cells. *Nat. Photon.* **13**, 460–466 (2019).
2. *Best Research-Cell Efficiency Chart* (NREL, accessed 3 January 2019); https://www.nrel.gov/pv/cell-efficiency.html.
3. Hörantner, M. T. et al. The potential of multijunction perovskite solar cells. *ACS Energy Lett.* **2**, 2506–2513 (2017).
4. Tennyson, E. M., Doherty, T. A. S. & Stranks, S. D. Heterogeneity at multiple length scales in halide perovskite semiconductors. *Nat. Rev. Mater.* **4**, 573–587 (2019).
5. Yin, W.-J., Shi, T. & Yan, Y. Unusual defect physics in $CH_3NH_3PbI_3$ perovskite solar cell absorber. *Appl. Phys. Lett.* **104**, 063903 (2014).
6. de Quilettes, D. W. et al. Impact of microstructure on local carrier lifetime in perovskite solar cells. *Science* **348**, 683–686 (2015).
7. Knight, A. J. et al. Electronic traps and phase segregation in lead mixed-halide perovskite. *ACS Energy Lett.* **4**, 75–84 (2019).
8. Jones, T. W. et al. Lattice strain causes non-radiative losses in halide perovskites. *Energy Environ. Sci.* **12**, 596–606 (2019).
9. Zhao, J. et al. Strained hybrid perovskite thin films and their impact on the intrinsic stability of perovskite solar cells. *Sci. Adv.* **3**, eaao5616 (2017).
10. Man, M. K. L. et al. Imaging the motion of electrons across semiconductor heterojunctions. *Nat. Nanotechnol.* **12**, 36–40 (2017).
11. Wong, E. L. et al. Pulling apart photoexcited electrons by photoinducing an in-plane surface electric field. *Sci. Adv.* **4**, eaat9722 (2018).
12. Saliba, M. et al. Cesium-containing triple cation perovskite solar cells: improved stability, reproducibility and high efficiency. *Energy Environ. Sci.* **9**, 1989–1997 (2016).
13. Wu, X. et al. Trap states in lead iodide perovskites. *J. Am. Chem. Soc.* **137**, 2089–2096 (2015).
14. Kollár, M. et al. Clean, cleaved surfaces of the photovoltaic perovskite. *Sci. Rep.* **7**, 695 (2017).
15. Nguyen-Truong, H. T. Electron inelastic mean free path at energies below 100 eV. *J. Phys. Condens. Matter* **29**, 215501 (2017).
16. Seah, M. P. & Dench, W. A. Quantitative electron spectroscopy of surfaces: a standard data base for electron inelastic mean free paths in solids. *Surf. Interface Anal.* **1**, 2–11 (1979).
17. Yang, Y. et al. Top and bottom surfaces limit carrier lifetime in lead iodide perovskite films. *Nat. Energy* **2**, 16207 (2017).
18. Rehman, W. et al. Photovoltaic mixed-cation lead mixed-halide perovskites: links between crystallinity, photo-stability and electronic properties. *Energy Environ. Sci.* **10**, 361–369 (2017).

19. Chen, S. et al. Atomic scale insights into structure instability and decomposition pathway of methylammonium lead iodide perovskite. *Nat. Commun*. **9**, 4807 (2018).
20. Stranks, S. D. et al. Recombination kinetics in organic–inorganic perovskites: excitons, free charge, and subgap states. *Phys. Rev. Appl*. **2**, 034007 (2014).
21. Wetzelaer, G.-J. A. H. et al. Trap-assisted non-radiative recombination in organic–inorganic perovskite solar cells. *Adv. Mater*. **27**, 1837–1841 (2015).
22. Tian, W. et al. Limiting perovskite solar cell performance by heterogeneous carrier extraction. *Angew. Chem. Int. Ed*. **55**, 13067–13071 (2016).
23. Frost, J. M., Whalley, L. D. & Walsh, A. Slow cooling of hot polarons in halide perovskite solar cells. *ACS Energy Lett*. **2**, 2647–2652 (2017).
24. Kirchartz, T., Markvart, T., Rau, U. & Egger, D. A. Impact of small phonon energies on the charge-carrier lifetimes in metal-halide perovskites. *J. Phys. Chem. Lett*. **9**, 939–946 (2018).
25. Chatterjee, R., Pavlovetc, I. M., Aleshire, K., Hartland, G. V. & Kuno, M. Subdiffraction infrared imaging of mixed cation perovskites: probing local cation heterogeneities. *ACS Energy Lett*. **3**, 469–475 (2018).
26. Whalley, L. D., Crespo-Otero, R. & Walsh, A. H-center and V-center defects in hybrid halide perovskites. *ACS Energy Lett*. **2**, 2713–2714 (2017).
27. Li, W., Liu, J., Bai, F.-Q., Zhang, H.-X. & Prezhdo, O. V. Hole trapping by iodine interstitial defects decreases free carrier losses in perovskite solar cells: a time-domain ab initio study. *ACS Energy Lett*. **2**, 1270–1278 (2017).
28. Motti, S. G. et al. Controlling competing photochemical reactions stabilizes perovskite solar cells. *Nat. Photon*. **13**, 532–539 (2019).
29. Park, J.-S., Calbo, J., Jung, Y.-K., Whalley, L. D. & Walsh, A. Accumulation of deep traps at grain boundaries in halide perovskites. *ACS Energy Lett*. **4**, 1321–1327 (2019).
30. Stranks, S. D. Nonradiative losses in metal halide perovskites. *ACS Energy Lett*. **2**, 1515–1525 (2017).
31. Correa-Baena, J.-P. et al. Homogenized halides and alkali cation segregation in alloyed organic–inorganic perovskites. *Science* **363**, 627–631 (2019).

Methods

Perovskite preparation

All perovskite films were prepared in Cambridge in a N_2-filled glove box. Thin films of $(Cs_{0.05}FA_{0.78}MA_{0.17})Pb(I_{0.83}Br_{0.17})_3$ were prepared from solutions containing formamidinium iodide (FAI) (1 M), methylammonium bromide (MABr) (0.2 M), PbI_2 (1.1 M), $PbBr_2$ (0.22 M) dissolved in anhydrous dimethylformamide/dimethyl sulfoxide (DMF:DMSO 4:1 (v:v)). CsI dissolved in DMSO (1.5 M) was then added to the precursor solution. $(Cs_{0.05}FA_{0.78}MA_{0.17})PbI_3$ thin films were prepared from precursor solutions containing FAI (1 M), PbI_2 (1.32 M) and MAI (0.2 M) in anhydrous DMF:DMSO 4:1 (v:v). CsI dissolved in DMSO (1.5 M) was then added to the precursor solution.

For the PEEM, PL and photothermal deflection spectroscopy (PDS) data presented in Fig. 1 and 4, and Extended Data Figs. 1, 3, 5, 6, 7 and 9–12 the precursor solution was spin coated onto ITO substrates (ranging in size from 0.8 cm × 0.8 cm to 1 cm × 1 cm) in two steps at 2,000 and 4,000 rpm for 10 and 35 s, respectively, with 100 µl of chlorobenzene added 30 s before the end of the second step. The films were then annealed at 100 °C for 1 h. In all our samples fabricated in this manner, we obtained film thicknesses of ~500 nm.

For the SED/PEEM and STEM-EDX/KPFM correlation data presented in Figs. 2, 3 and Extended Data Fig. 8, the perovskite solution was diluted in anhydrous DMF:DMSO 4:1 (v:v) (2:1 ratio of dilutant to precursor solution) and then spin-coated on Agar Scientific SiN TEM grids (3 mm diameter) (product number: AGS171-2) in two steps at 2,000 and 6,000 rpm for 10 s and 35 s respectively, with 20 µl of chlorobenzene added 30 s before the end of the second step. In all our samples fabricated in this manner, we obtained film thicknesses of ~200 nm required for electron transparency.

Fiducial Au markers were deposited by spin-coating a suspension of Au nanoparticles in chlorobenzene at 1,000 rpm for 20 s, which were used for spatial alignment of the sample between different measurement techniques. These uniquely and randomly shaped markers are small (few micrometres in size), dilute in distribution (few markers per square millimetre), and measurements were made several micrometres away from the marker itself. As a result, and as confirmed by control experiments, these Au markers do not affect our measurements[8]. Samples for PEEM measurements were then sealed in air-tight packaging and sent to Okinawa Institute of Science and Technology, where they were stored and re-opened in a N_2 glovebox. Samples were loaded onto the PEEM sample holder inside the N_2 glovebox and transferred to the ultra-high-vacuum (UHV) system through a vacuum/N_2-compatible suitcase.

Devices used to obtain the data in Extended Data Fig. 2 were prepared as follows. ITO substrates were cleaned with Hellmanex III soap, DI water, acetone and isopropanol with sonication for 30 min each. UV ozone was used to clean the substrate and improve the surface wetting for 15 min before the deposition of the hole-transporting layer. For the poly(triaryl amine) (PTAA) layer, 5 mg ml^{-1} PTAA (M_W 19,000) in anhydrous toluene was spun on to the ITO substrate at 4,000 rpm for 30 s. The film was then annealed on a hotplate at 100 °C for 10 min. Because of the hydrophobic nature of PTAA, we spun a poly[(9,9-bis(30-((*N*,*N*-dimethyl)-*N*-ethylammonium)-propyl)-2,7-fluorene)-alt-2,7-(9,9-dioctylfluorene)] dibromide (PFN-P2) solution (1-Material, 0.5 mg ml^{-1}) to improve the wetting and passivate the interfaces[32].

To fabricate the perovskite film, the $(Cs_{0.05}FA_{0.78}MA_{0.17})Pb(I_{0.83}Br_{0.17})_3$ perovskite precursor (prepared as above) was spin-coated on the substrate in a two-step process: 1,000 rpm for 10 s and 6,000 rpm for 20 s. Chlorobenzene (100 µl) was introduced in the middle of the film 5 s before the end of the second step, and the perovskite layer was then annealed at 100 °C for 1 h. Deposition of the electron-transporting layer was completed by spinning [6,6]-phenyl-C61-butyric acid methyl ester (PCBM) (20 mg ml^{-1}, Merck) on top of perovskite film at 1,200 rpm for 30 s. The bathocuproine (BCP) solution (0.5 mg ml^{-1}, Alfa) was dynamically spin-coated on the PCBM layer to form a buffer layer. The Ag electrode was thermally deposited at a rate of 0.1 Å s^{-1} for the first 2 nm and then a rate of 1 Å s^{-1} thereafter to achieve a thickness of 100 nm.

Device characterization

For current density versus voltage (*J*–*V*) measurements, a source meter (Keithley 2636A) was used to record the parameter. A standard silicon reference diode (no filter) was used to calibrate the light intensity to one Sun AM1.5 G of 100 mW cm^{-2}. The mismatch factor of 1.13 for a bandgap of 1.6 eV was accounted for during calibration. A 450-W xenon lamp equipped with Abet solar simulator was used as a light source. The scan of the *J*–*V* curve was from −0.1 V to 1.2 V (forward scan) and 1.2 V to −0.1 V (reverse scan) with a scan rate of 100 mV s^{-1} and a step size of 0.02 V. A mask with an aperture size of 8.3 mm^2 was used. All device measurements were conducted in air without any encapsulation, pre-bias or light-soaking conditions.

TR-PEEM set-up

The source laser used for PEEM and TR-PEEM imaging was a 4-MHz, 650-nJ Ti:sapphire oscillator (FemtoLasers XL:650) delivering 45 fs pulses at 800 nm. The laser is split into two paths; one path is used for generating the UV pulses for PEEM imaging, and the other is used for the pump pulses for excitation in time-resolved measurements. The 4.65-eV UV pulses are generated as the third harmonic of the 1.55-eV (800-nm) fundamental by sum frequency generation of the fundamental and the 3.10-eV (400-nm) second harmonic. The 6.2-eV UV pulses are then generated via sum frequency generation of the 4.65-eV (266-nm) third harmonic and the 1.55-eV (800-nm) fundamental[33]. The pump is sent to a variable 200-mm delay stage which controls the time delay between pump and probe pulse arrival at the sample. The probe and pump lasers are focused into the ultra-high-vacuum chamber of the PEEM instrument (SPELEEM, Elmitec GmbH), where they are incident at a grazing angle of about 17° on the sample. The pump spot size was approximately 70 µm full-width half-maximum (FWHM) (short axis of ellipse) at the sample, whereas the probe was loosely focused to about 250 µm FWHM to provide more uniform imaging. The UV pulses were set to p-polarization whereas pump pulses were s-polarized. Typical UV pulse fluences used were approximately <100 nJ cm^{-2} for the third harmonic (4.65 eV) and <10 nJ cm^{-2} for the fourth harmonic (6.2 eV). UV pulse fluences were chosen as a balance between PEEM intensity and space-charge effects[34]; generally, the UV fluence was reduced to a level at which no or minimal broadening of the photoemission spectrum could be observed. The 1.55-eV pump-pulse fluence used for time-resolved measurements was about 20 µJ cm^{-2} for $(Cs_{0.05}FA_{0.78}MA_{0.17})PbI_3$ thin-film samples. The overall temporal resolution of our experiment was estimated to be about 300 fs from the measured pump-probe temporal overlap in TR-PEEM[10,11].

PEEM image acquisition and processing

Measurements were performed at room temperature in the UHV chamber of the PEEM instrument, with a base pressure of 10^{-10} torr or better. TR-PEEM images and PEEM images of the trap sites were taken with third-harmonic (4.65-eV) pulses, a field of view (FOV) of 10 µm, and no contrast aperture. Energy resolved images and photoemission spectra were taken using fourth-harmonic (6.2-eV) pulses, no contrast aperture, and with the hemispherical energy analyser slit set to 250-meV energy resolution. The Fermi level of the system was referenced to the high kinetic energy edge of nearby gold markers deposited on the sample.

Higher-resolution PEEM images of the traps and film morphology were taken with a FOV of 7.5 µm and a 100-µm contrast aperture. PEEM images of the surface morphology were taken with 6.2-eV pulses, the energy analyser set to 250-meV energy resolution and integrated at the valence-band edge (peak centred roughly at $E - E_F = -2$ eV in the measured photoemission spectra). With the contrast aperture inserted,

we could achieve a spatial resolution in PEEM of about 20 nm, as estimated from the line profiles in Fig. 1e using a criterion of 84% to 16% of the image intensity across the edge of the trap. Images taken without the contrast aperture inserted had a resolution as good as about 40 nm.

All PEEM images were corrected using a flat field method to remove the non-uniformity in the instrument main channel plate and phosphorescent screen. For time-resolved measurements, typical image conditions for a single frame (single pump-probe delay step) were 4-s exposure with two averages. To reduce artefacts from sample drift and laser intensity fluctuations, TR-PEEM experiments were taken with multiple repeat scans (five repeats for the data shown in Fig. 4). Any sample drift in position or slow intensity variations over the repeated scans are then corrected during analysis before averaging the scans together. For extracted TR-PEEM intensity curves, intensity fluctuations of the laser are reduced at each delay step by normalizing the TR-PEEM signal to the photoemission intensity of the gold markers within the same image used as position references.

Displayed TR-PEEM images are averaged with a rolling average window of five frames between delay steps to smooth image-to-image noise. To view the changes due to pump excitation, the TR-PEEM images shown have been subtracted by the average of the non-photoexcited PEEM images taken at a negative pump-probe delay (that is, probe arriving before pump excitation) during the measurement sequence.

For energy-resolved images, the spatial variation of the measured kinetic energy due to the hemispherical analyser dispersion was corrected using a uniform area (for example, Au marker) as a reference. Exposure times for energy-resolved images (for photoemission spectroscopy) with the fourth harmonic were 20 s with four averages per image for the data shown in Fig. 1a. The background noise of the instrument was removed by subtracting images at lower kinetic energy where there is no photoemission intensity. Spatially resolved photoemission spectra are extracted from selected areas of the sequence of images at different kinetic energies (see Extended Data Fig. 6).

Analysis of trapping dynamics

As stated in the main text, we did not observe any TR-PEEM signals related to free carriers in our measurements here. Free carriers in the conduction band would have resulted in a sharp transient (pulse-width-limited) increase in the measured TR-PEEM signal, which was not observed in these measurements, as well as in attempts at spectroscopic (energy-resolved) TR-PEEM measurements. There are several possible reasons that the signal from free carriers in the conduction band could not be observed, but it is currently unclear which is the exact cause. Three likely issues are: having an unfavourable transition probability for the probe photon; momentum conservation in the photoemission processes; and a low density of states at the band edge. For the first issue, it is possible that there is no allowed optical transition between the conduction band minimum and a state above the vacuum level at the energy of our probe photon, making the signal too weak to detect. This transition must conserve energy, momentum and spin, which is a general requirement of photoemission spectroscopy[35,36]. The second issue follows from this requirement, where for an FA-based perovskite at room temperature (cubic phase), the bandgap was calculated to be at the high-momentum R point in the Brillouin zone[37].To maintain momentum conservation, this would require an additional photon energy of about 11 eV (assuming a cubic lattice with $a \approx 6.3$ Å) on top of the energy needed to overcome the work function and binding energy. With probe energies of only 4.65 eV and 6.2 eV, we cannot directly probe such a high-momentum point in the Brillouin zone, and this would prevent us from observing free carriers in the conduction or valence bands. The third issue could be due to the low density of states (DOS) at the bandgap, which has been discussed previously[38]. This could result in time-resolved signals being very small and difficult to detect above the background photoemission signal from other states.

We have checked for effects due to surface band bending. Measurements comparing surface photovoltage shifts of the photoemission spectrum (between negative and positive pump-probe time delays) under the same experimental conditions have shown only small shifts of a few tens of millielectronvolts, which is below the energy resolution of the analyser. Therefore, band-bending effects here are likely to be small and should not affect either the static or time-resolved photoemission measurements discussed here.

Now, we discuss in more detail the analysis used for the measured hole-trapping dynamics. Unless stated otherwise, TR-PEEM curves are fitted with a double-exponential equation:

$$y(t) = A_1(\exp\{-t/\tau_1\} - 1) + A_2(\exp\{-t/\tau_2\} - 1)$$

where A_1 and A_2 are amplitudes, and τ_1 and τ_2 are the fast and slow time constants, respectively. Owing to its low amplitude, the τ_1 time constant is not always well resolved in these measurements. Although we use a bi-exponential function here for a better fit, we still observe the same lack of dependence of the trapping time for both single-exponential and stretched exponential fits (see Extended Data Fig. 11). Across several spatially averaged measurements on $(Cs_{0.05}FA_{0.78}MA_{0.17})PbI_3$ samples, the mean amplitudes and time constants are $A_1 = 4.0 \pm 2.0$, and $A_2 = 12 \pm 5$, $\tau_1 = 9 \pm 4$ ps and $\tau_2 = 81 \pm 21$ ps, where the error is the standard deviation across six different measurements.

Next, we describe the analysis used to compare TR-PEEM signals between different trap sites intensities. Based on the monomolecular Shockley–Read–Hall trapping formalism, the trapping dynamics should depend on the trap density and thus the initial photoemission signal I_0 (refs. [39,40]). To compare across all the trap sites within the PEEM image, we then implement a binning procedure to compare the TR-PEEM signal between groups of trap sites, which is outlined below. First, any artefacts or unwanted signals, such as the edge of the image or the gold position markers, are masked from the image (Extended Data Fig. 12a). The image is then processed by using an intensity threshold, and a connectivity algorithm is used to identify all the trap sites within the image and sort them based on their intensity (Extended Data Fig. 12b). The TR-PEEM signal is then extracted separately for each binned intensity level and fitted with a double-exponential decay. The TR-PEEM signals (coloured dots) and corresponding fits (grey lines) for four of the bins are shown in Extended Data Fig. 12c and are offset for clarity. The resulting time constants and amplitudes as a function of the non-photoexcited PEEM intensity are shown in Extended Data Fig. 12d and e, respectively, with the error bars representing the fitting error for each intensity bin. We note that owing to its low amplitude, the τ_1 time constant is not reliably fitted for many bins. Any empty bins and bins with no signal (that is, the fit routine fails to converge) are excluded from Extended Data Fig. 12d and e. We also show the fitting results using single-exponential and stretched exponential functions in Extended Data Fig. 11. From this analysis, we find that the trapping time constants measured (Extended Data Fig. 12d) are independent of the trap intensity, indicating that the trapping kinetic is not following the expected Shockley–Read–Hall behaviour and therefore must be limited by a slower mechanism.

Photoluminescence measurements

PL maps on $(Cs_{0.05}FA_{0.78}MA_{0.17})Pb(I_{0.83}Br_{0.17})_3$ for correlation with PEEM images (Fig. 1c and Extended Data Fig. 7e) were acquired on a Leica TCS SP8 STED3X confocal microscope. The excitation source was a continuous-wave 442-nm diode laser with an intensity of about 2 μW (~1.7 kW cm^{-2}, assuming a diffraction-limited probe), focused through an oil objective (100× magnification, 1.4 NA). PL was collected across a 15 μm × 15 μm region (15-nm step, 200-Hz scan speed). Maps were

acquired after regions of interest had been identified and measured in PEEM, using gold particles as fiducial markers.

PL maps on $(Cs_{0.05}FA_{0.78}MA_{0.17})Pb(I_{0.83}Br_{0.17})_3$ deposited on a SiN X-ray window and perovskite devices (Extended Data Fig. 2) were acquired using a Picoquant MicroTime 200 confocal microscope. The excitation source was a pulsed 404-nm laser (2-MHz repetition rate), focused through an objective lens (100× magnification, 0.9 NA) with an average power of 1.3 nW (~550 mW cm^{-2}, with a measured probe size of ~550 nm). PL was collected across a region 15 µm × 15 µm (59-nm pixel size, 300-µs dwell time).

PL maps on $(Cs_{0.05}FA_{0.78}MA_{0.17})PbI_3$ films were performed in a confocal microscope configuration (Nanofinder 30) using a 532-nm excitation laser with an intensity of 50 nW (~9.7 W cm^{-2} assuming a diffraction-limited probe) focused through a 0.8 NA (100×) objective. PL maps were acquired by scanning the laser spot with a galvanic mirror in 100-nm steps. Spectroscopic measurements (PL in Extended Data Fig. 1) on both film compositions were performed in the same set-up with 5-nW intensity (~970 mW cm^{-2}) and averaged over a scan area of ~6 × 6 $µm^2$. For generating the overlay in Fig. 4a (and Extended Data Fig. 10), the PEEM and PL images are overlaid and aligned using the gold marker as a position reference.

All PL measurements correlated with PEEM were performed in air after PEEM and TR-PEEM experiments and were aligned to the same sample location via fiducial gold markers placed during film preparation.

Spectrally resolved PL images (Extended Data Fig. 3d) and the accompanying spectra (Extended Data Fig. 3c) were acquired with an IMA wide-field hyperspectral microscope (Photon Etc). Continuous-wave excitation was provided by a 405-nm laser with intensity below 3 suns (250 mW cm^{-2}), through a 20× objective lens. Spatially averaged PL spectra were extracted from each image and local spectra (Extended Data Fig. 3c inset) were extracted from the highlighted regions of 'PEEM exposure' and 'no PEEM exposure'. Optical reflectance images (Extended Data Fig. 3b) were measured on the same set-up using white light illumination.

Absorption measurements

Photothermal deflection spectroscopy measurements were acquired on a custom-built set-up by monitoring the deflection of a fixed-wavelength (670-nm) laser probe beam after absorption of each monochromatic pump wavelength by a thin film immersed in an inert liquid, FC-72 Fluorinert (3M)

Absorption measurements to determine quantitative changes in films after shipping and extreme PEEM exposure measurements (Extended Data Fig. 3a) were performed with a Shimadzu UV-3600 Plus with ISR-603 integrating sphere attachment. Measurements were carried out in transmittance configuration and referenced to an ITO/glass substrate.

SED measurements

SED microscopy involves recording a 2D electron diffraction pattern at every probe position as a focused electron beam is scanned across the sample. SED data were acquired on the JEOL ARM300CF E02 instrument at ePSIC, Diamond Light Source. The key capability offered by the E02 instrument at ePSIC is the Merlin/Medipix pixelated STEM detector for fast SED. Using this highly sensitive detector and the following experimental parameters: accelerating voltage 300 kV; nanobeam alignment (convergence angle ~1 mrad); electron probe ~4 nm; probe current ~2 pA; scan dwell time 1 ms; and camera length 15 cm, we can achieve an electron dose per scan of ~6.25 e $Å^{-2}$ when approximating the beam shape as a circle with a diameter of 4 nm. This accumulated dose is over an order of magnitude lower than the reported damage threshold for $MAPbI_3$ (100 e $Å^{-2}$)[19,41]. SED diffraction data were analysed in pyXem[42] (an open-source Python library for crystallographic electron microscopy). In the main text, we refer to virtual bright-field images, which are reconstructed from SED data by plotting the intensity integrated around the direct beam as a function of probe position. The resulting image is formed exclusively by directly transmitted electrons.

Analysis of diffraction data

All diffraction patterns obtained from the bulk parent material can be indexed as a cubic $FAPb(I_{0.83},Br_{0.17})_3$ crystal with a lattice parameter of ~6.30 Å. This is consistent with Vegard's law for $FAPbI_xBr_{1-x}$ and a random alloy over the predominantly cubic FA-rich sites in the $(Cs_{0.05}FA_{0.78}MA_{0.17})Pb(I_{0.83}Br_{0.17})_3$ composition. Any variations that would occur in diffraction patterns between the simple $FAPb(I_{0.83},Br_{0.17})_3$ cubic model used for indexation here and the more complex $(Cs_{0.05}FA_{0.78}MA_{0.17})Pb(I_{0.83}Br_{0.17})_3$ structure of the samples are minor and beyond the reciprocal-space resolution of our techniques. In SED, under these operating conditions, one pixel on the Merlin/Medipix pixelated STEM detector is ~0.014 $Å^{-1}$. Diffraction patterns are calibrated with an Au cross grating.

SED data were treated with principal component analysis (PCA) to denoise the data. PCA sorts the signal into orthogonal components (linear combinations of variables) in decreasing order of variance. The high-variance components constitute the data's primary features, whereas low-variance components represent weaker contributions to the data. The number of high-variance components (primary features) was estimated by plotting the explained variance of the data set against the component index (Extended Data Fig. 8d,f) and detecting the point at which the scree plot becomes linear by using the knee-finding technique of ref. [43]. Non-negative matrix factorization (select loading maps shown in Fig. 3b,f) was then performed with the output dimension specified by the PCA scree plot. For the homogeneous grain shown in Fig. 3b, an output dimension of 3 was used (Extended Data Fig. 8d), whereas for the inhomogeneous grain shown in Fig. 3f, an output dimension of 5 was used (Extended Data Fig. 8f)[44].

For the inhomogeneous grain, the vector lengths of 0.898 $Å^{-1}$ and 1.116 $Å^{-1}$ (marked as 1 and 2 respectively in Extended Data Fig. 8g) compare closely to theoretical lengths of the cubic (440) and (444) reflections in cubic $FAPb(I_{0.83}Br_{0.17})_3$, which are 0.902 $Å^{-1}$ and 1.099 $Å^{-1}$ respectively. In this respect, the component diffraction pattern from the compositionally inhomogeneous grain is similar to a (110) zone axis pattern from cubic $FAPb(I_{0.83}Br_{0.17})_3$ and may be consistently indexed as pseudo-cubic. However, crucially, the (100) and (110) type reflections are not detectable, and the angle between the (200) and (220) planes (marked as θ in Extended Data Fig. 8g) is 87.6° instead of the nominal 90° for the cubic parent material. Similarly, the diffraction pattern is geometrically close to the 101 zone axis of PbI_2, but the differences between experimental and theoretical measured diffraction vector lengths and angles are substantially larger than in the successfully indexed bulk parent material. It is difficult to construct an atomic model based on either the [110] or [101] zone axes as a starting point that accounts for all diffraction measurements from the compositionally inhomogeneous grains; further work will be required to determine the local atomic structure unambiguously.

STEM/EDX measurements

HAADF-STEM images and STEM-EDX spectrum images were acquired with an FEI Tecnai Osiris (S)TEM equipped with a high-brightness Schottky X-FEG gun and a Bruker Super-X EDX system composed of four silicon drift detectors, each approximately 30 mm^2 in area and placed symmetrically around the optic axis, achieving a total collection solid angle of ~0.9 sr. Spectrum images were recorded using a 70-µm C2 aperture at an accelerating voltage of 200 kV, a beam current of ~250 pA, a spatial sampling of 10 nm per pixel and a dwell time of 50 ms per pixel. All data were acquired with TEM Imaging Analysis (TIA) and analysed with Hyperspy[45]. STEM-EDX was performed last, as it requires the highest probe current to generate meaningful data.

STEM-EDX analysis

STEM-EDX data were analysed in the open source Python package Hyperspy[45]. To improve the signal-to-noise ratio of the spectra, the energy axis was rebinned by four, and the data were treated with PCA for denoising. Briefly, as above, PCA sorts the signal into orthogonal components (linear combinations of variables) in decreasing order of variance. The high-variance components constitute the data's primary features, whereas low-variance components represent weaker contributions to the data. By removing the low-variance components, PCA greatly increases signal-to-noise ratio while retaining almost all variance, thus preserving statistical significance[46]. Ratio maps were then constructed by dividing the appropriate maps of peak intensity by each other.

KPFM measurements

KPFM was performed on a Dimension Icon Large-Sample tip-scanning AFM from Bruker. Here, all KPFM maps were 512 × 512 pixels acquired in frequency-modulated KPFM imaging mode at a typical scan rate of 0.3–0.4 Hz. For our measurements, we used Pt–Ir coated Si probes from Bruker, (model: SCM-PIT) which have an average resonant frequency of 75 kHz and spring constant of 2.8 N m^{-1}. All measurements were performed in the dark and in ambient atmospheric conditions. Perovskite samples deposited on both ITO and SiN substrates (Extended Data Fig. 2) were KPFM mapped. Variations in voltage of comparable magnitudes and spatial distributions are observed on both substrates. We note that the difference in CPD observed between the regions at a trap site, and away from a trap site, is similar to the energy resolution of our PEEM set-up (~150–200 meV).

SEM measurements

SEM imaging was performed at electron energy 5 kV with a LEO Gemini 1530VP FEG-SEM.

AFM measurements

AFM measurements (Fig. 1f) were obtained with a Bruker ICON3-OS1707 microscope in tapping mode.

X-ray diffraction measurements

X-ray diffraction (XRD) data were acquired at synchrotron beamline I14 of the Diamond Light Source using a 20-keV monochromatic X-ray beam (λ = 0.619 nm). Diffraction data were recorded on an Excalibur 3M detector consisting of three Medipix 2,048 × 512 pixel arrays. 2D detector images were calibrated with a CeO_2 calibrant and radially integrated in The Data Analysis WorkbeNch (DAWN). The XRD data were averaged over a sample area of 30 × 30 μm^2.

Exposure controls

To check the material stability and sensitivity to exposure we show measurements, including absorption, emission and structural measurements, on $(Cs_{0.05}FA_{0.78}MA_{0.17})Pb(I_{0.83}Br_{0.17})_3$ samples freshly made, after shipping, and after intense and long-term exposure to our PEEM experimental conditions, namely the UV laser probe and UHV. The PEEM exposure in these measurements was ~7 h long with ~100 nJ cm^{-2} per pulse of UV light (total dose ~10 kJ cm^{-2}). This long-term and intense exposure to PEEM conditions for the control measurements aimed to stress the samples in an extreme way in order to begin seeing degradation effects. In contrast, typical experimental conditions were ~20 min of UV exposure at less than 100 nJ cm^{-2} per pulse (<0.5 kJ cm^{-2} total dose for a single time-resolved measurement), or ~1 h of less than 10 nJ cm^{-2} per pulse (<0.3 kJ cm^{-2} total dose for spectroscopic PEEM measurements). Thus the doses on the sample during our actual measurement conditions are over an order of magnitude lower than during the exposure controls and do not affect the results of our experiments.

Absorption. In Extended Data Fig. 3a, we show the absorption of fresh films (black), after shipping (red), and after intense and long-term exposure to PEEM conditions (blue). We see no appreciable changes in the absorption edge.

Optical reflectivity. In Extended Data Fig. 3b, we show the optical reflectivity image of a sample, part of which has been exposed to intense and long-term PEEM conditions. There is no visible change in the sample surface after the exposure, in agreement with the optical absorption measurements.

Photoluminescence. In spectrally resolved measurements (Extended Data Fig. 3c), we see that there is no appreciable change in the central wavelength or the emission width of the PL from fresh films (black), after shipping (red), and after exposure to the intense and long-term PEEM conditions (blue). We do, however, see a ~30% decrease in PL intensity after the extended PEEM exposure (Extended Data Fig. 3c inset). This decrease is consistent with previous literature in which PL yield is known to decrease owing to effects such as light-induced ion migration under vacuum conditions[28,47]. Again, we note that for the reported experiments in the main text, the UV exposure is more than an order of magnitude lower in dose and thus its effects are much smaller (<1% as shown below).

PEEM maps. During the intense and long-term PEEM exposure (UV + UHV), we can monitor the PEEM image and the corresponding intensity of the trap sites over time. By comparing before and after PEEM images (Extended Data Fig. 3e and f), we see that the spatial distribution of the traps is unchanged. We do find that there is an increase of ~30–40% in the intensity of the traps after the ~7-h exposure to UV light (Extended Data Fig. 3g). This corresponds well with the measured reduction in PL after the exposure.

XRD measurements under regular exposure. Lastly, we discuss control checks done under regular PEEM exposure conditions. First, we show XRD measurements averaged over an area ~30 × 30 μm^2 (Extended Data Fig. 4a) on freshly made samples (black curve) and on samples which were shipped and imaged in PEEM (blue curve). We observe no differences in the crystalline quality of the samples.

PEEM measurements under regular exposure. We also show a set of repeated TR-PEEM pump-probe scans ($(Cs_{0.05}FA_{0.78}MA_{0.17})Pb(I_{0.83}Br_{0.17})_3$ sample, 1.55-eV pump, 4.65-eV probe), where we plot the real time during the measurement on the bottom x-axis (Extended Data Fig. 4b). For the sequence of five repeated scans, by comparing the intensity of the negative time delay points at the start of each scan, we see that there is a small change of about ~4% (dashed grey lines) over the total measurement time of ~80 min. This rate of change matches our observation from the more extensive exposure (~30% in 7 h) and shows that for a single measurement scan (<20 min), there is a negligible change (<1%) in the trap intensity.

Data availability

The data that support the findings of this study are available at https://doi.org/10.17863/CAM.48273 or from the corresponding authors upon request.

32. Stolterfoht, M. et al. Visualization and suppression of interfacial recombination for high-efficiency large-area pin perovskite solar cells. *Nat. Energy* **3**, 847–854 (2018).
33. Rotermund, F. & Petrov, V. Generation of the fourth harmonic of a femtosecond Ti:sapphire laser. *Opt. Lett.* **23**, 1040–1042 (1998).
34. Buckanie, N. M. et al. Space charge effects in photoemission electron microscopy using amplified femtosecond laser pulses. *J. Phys. Condens. Matter* **21**, 314003 (2009).
35. Hüfner, S. *Photoelectron Spectroscopy: Principles and Applications* (Springer, 2003).

36. Damascelli, A. Probing the electronic structure of complex systems by ARPES. *Phys. Scr*. **2004**, T109 (2004).
37. Pan, Y. Y., Hsu, C. H., Huang, L. W., Dou, K. P. & Kaun, C. C. First-principles study on electronic structures of $FAPbX_3$ (X = Cl, Br, I) hybrid perovskites. *J. Adv. Nanomater*. **1**, https://doi.org/10.22606/jan.2016.11004 (2016).
38. Endres, J. et al. Valence and conduction band densities of states of metal halide perovskites: a combined experimental–theoretical study. *J. Phys. Chem. Lett*. **7**, 2722–2729 (2016).
39. Shockley, W. & Read, W. T. Statistics of the recombinations of holes and electrons. *Phys. Rev*. **87**, 835–842 (1952).
40. Fukumoto, K., Yamada, Y., Koshihara, S. & Onda, K. Lifetimes of photogenerated electrons on a GaAs surface affected by nanostructural defects. *Appl. Phys. Express* **8**, 101201 (2015).
41. Rothmann, M. U. et al. Structural and chemical changes to $CH_3NH_3PbI_3$ induced by electron and gallium ion beams. *Adv. Mater*. **30**, 1800629 (2018).
42. Johnstone, D. N. et al. *pyxem/pyxem: pyxem 0.10.0* (Zenodo, 2019); https://zenodo.org/record/3533653#.XnLPk4gza71.
43. Satopaa, V., Albrecht, J., Irwin, D. & Raghavan, B. in *2011 31st International Conf. on Distributed Computing Systems Workshops* 166–171 (2011); https://doi.org/10.1109/ICDCSW.2011.20.
44. Martineau, B. H., Johnstone, D. N., van Helvoort, A. T. J., Midgley, P. A. & Eggeman, A. S. Unsupervised machine learning applied to scanning precession electron diffraction data. *Adv. Struct. Chem. Imaging* **5**, 3 (2019).
45. de la Peña, F. et al. *hyperspy/hyperspy v1.4.1* (Zenodo, 2018); https://doi.org/10.5281/zenodo.1469364.
46. Cacovich, S. et al. Unveiling the chemical composition of halide perovskite films using multivariate statistical analyses. *ACS Appl. Energy Mater*. **1**, 7174–7181 (2018).
47. Kim, G. Y. et al. Large tunable photoeffect on ion conduction in halide perovskites and implications for photodecomposition. *Nat. Mater*. **17**, 445–449 (2018).

Acknowledgements T.A.S.D. acknowledges support of a National University of Ireland (NUI) Travelling Studentship. The work received funding from the European Research Council (ERC) under the European Union's Horizon 2020 research and innovation programme (HYPERION, grant agreement no. 756962). A.J.W., S.K., V.P., C.E.P., E L.W., J.M., M.K.L.M. and K.M.D. acknowledge that this work was supported by the Femtosecond Spectroscopy Unit of the Okinawa Institute of Science and Technology Graduate University. The authors acknowledge the support for this work from the Imaging Section and Engineering Support Section of the Okinawa Institute of Science and Technology Graduate University. This work was supported by JSPS KAKENHI Grant Number JP19K05637. S.M. acknowledges funding from the Summer Fellowship Programme of the Japan Society for the Promotion of Science and from a UK Engineering and Physical Sciences Research Council (EPSRC) studentship. S.D.S. acknowledges the Royal Society and Tata Group (UF150033). We thank Diamond Light Source and beamline scientists J. Parker, P. Quinn, M. Danaie and T. Slater for access and support in use of beamline I14 (proposal nos. sp19023-1 and sp19023-2) and the electron Physical Science Imaging Centre (ePSIC instrument E02 and proposal nos. EM19793-1, EM19793-2) that contributed to the results presented here. F.U.K. thanks the Jardine Foundation and Cambridge Trust for a doctoral scholarship. P.A.M. thanks the EPSRC for financial support under grant no. EP/R008779/1. E.M.T. acknowledges funding from the EPSRC under grant reference EP/R023980/1 and has received funding from the European Union's Horizon 2020 research and innovation programme under the Marie Skłodowska-Curie grant agreement no. 841265. S.D.S. and E.M.T. acknowledge funding from the EPSRC grant "Centre for Advanced Materials for Integrated Energy Systems (CAM-IES)" EP/P007767/1 and Cambridge Royce facilities grant EP/P024947/1. M.A. acknowledges funding from the European Union's Horizon 2020 research and innovation programme under the Marie Skłodowska-Curie actions grant agreement no. 841386. Y.-H.C. acknowledges support of a Cambridge Trust-Taiwan scholarship. M.A.-J. thanks Cambridge Materials Limited, Wolfson College, University of Cambridge, and EPSRC (grant no. EP/M005143/1) for their funding and technical support. Z.A.-G. acknowledges funding from a Winton Studentship and an ICON Studentship from the Lloyd's Register Foundation. This work was supported by a National Research Foundation of Korea grant funded by the Korean government (MSIT) (no. 2018R1C1B6008728).

Author contributions T.A.S.D. collected, analysed and interpreted SED, XRD, SEM, HAADF and STEM-EDX data, prepared samples and performed microscopy correlations. A.J.W. collected, analysed and interpreted PEEM and TR-PEEM data, and collected confocal PL data. S.M. prepared samples, collected confocal and hyperspectral PL data, collected optical absorption data, analysed data and assisted in interpretation of data. D.N.J. collected, analysed and interpreted SED data. V.P. built the laser set-up for the TR-PEEM measurements. E.M.T. collected and analysed KPFM data. S.K. collected, analysed and interpreted PEEM and AFM data. F.U.K. collected and analysed STEM-HAADF images and STEM-EDX data. M.A. collected hyperspectral PL data. M.A-J. prepared samples and performed PDS measurements. Z.A-G. prepared samples. Y.-H.C. prepared and tested devices and collected SEM data. C.E.P. and E L.W. assisted in interpretation of data. J.M. assisted in interpretation of data and built the laser set-up for the TR-PEEM measurements. M.K.L.M. assisted in analysis and interpretation of data. G.D. and C.D. supervised F.U.K.. P.A.M. supervised D.N.J. and aided in interpretation of SED data. K.M.D. supervised A.J.W, V.P., S.K., E L.W., C.E.P., J.M. and M.K.L.M. S.D.S supervised T.A.S.D., S.M., E.M.T., Y.-H.C. and M.A. A.W., J.-S.P. and Y.-K.J. provided input on data interpretations. S.D.S. and K.M.D. conceived and designed the work. All authors contributed to writing the manuscript.

Competing interests S.D.S. is a co-founder of Swift Solar, Inc.

Additional information

Supplementary information is available for this paper at https://doi.org/10.1038/s41586-020-2184-1.

Correspondence and requests for materials should be addressed to K.M.D. or S.D.S.

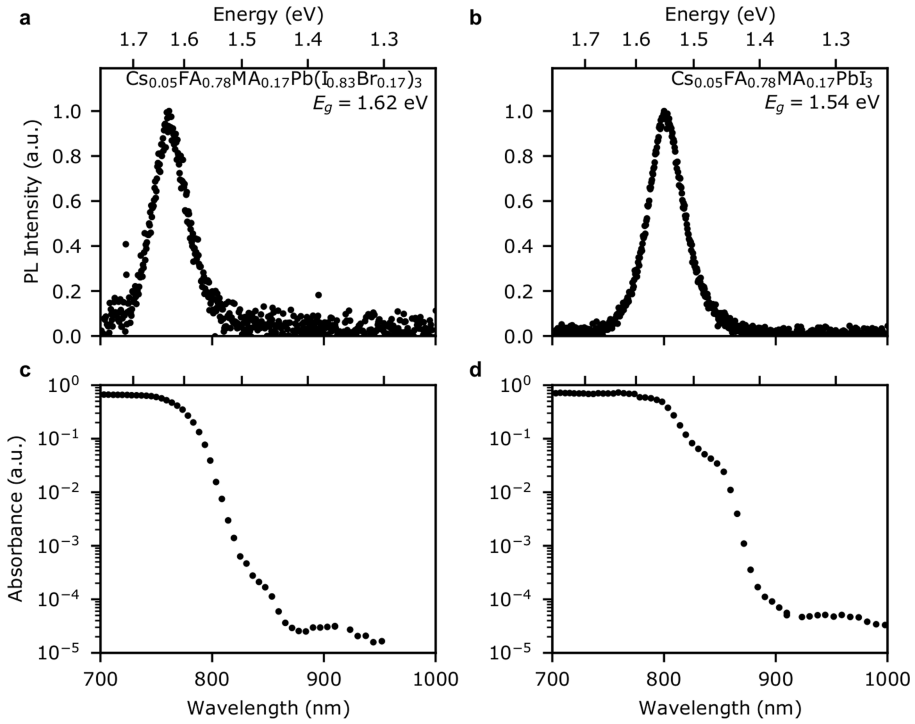

Extended Data Fig. 1 | Optical spectroscopy of mixed-cation films. a, **b**, PL spectra with 532-nm excitation of (**a**) $(Cs_{0.05}FA_{0.78}MA_{0.17})Pb(I_{0.83}Br_{0.17})_3$ and (**b**) $(Cs_{0.05}FA_{0.78}MA_{0.17})PbI_3$ films. **c**, **d**, Photothermal deflection spectroscopy (PDS) of (**c**) $(Cs_{0.05}FA_{0.78}MA_{0.17})Pb(I_{0.83}Br_{0.17})_3$ and (**d**) $(Cs_{0.05}FA_{0.78}MA_{0.17})PbI_3$ films, showing a negligible sub-bandgap absorption.

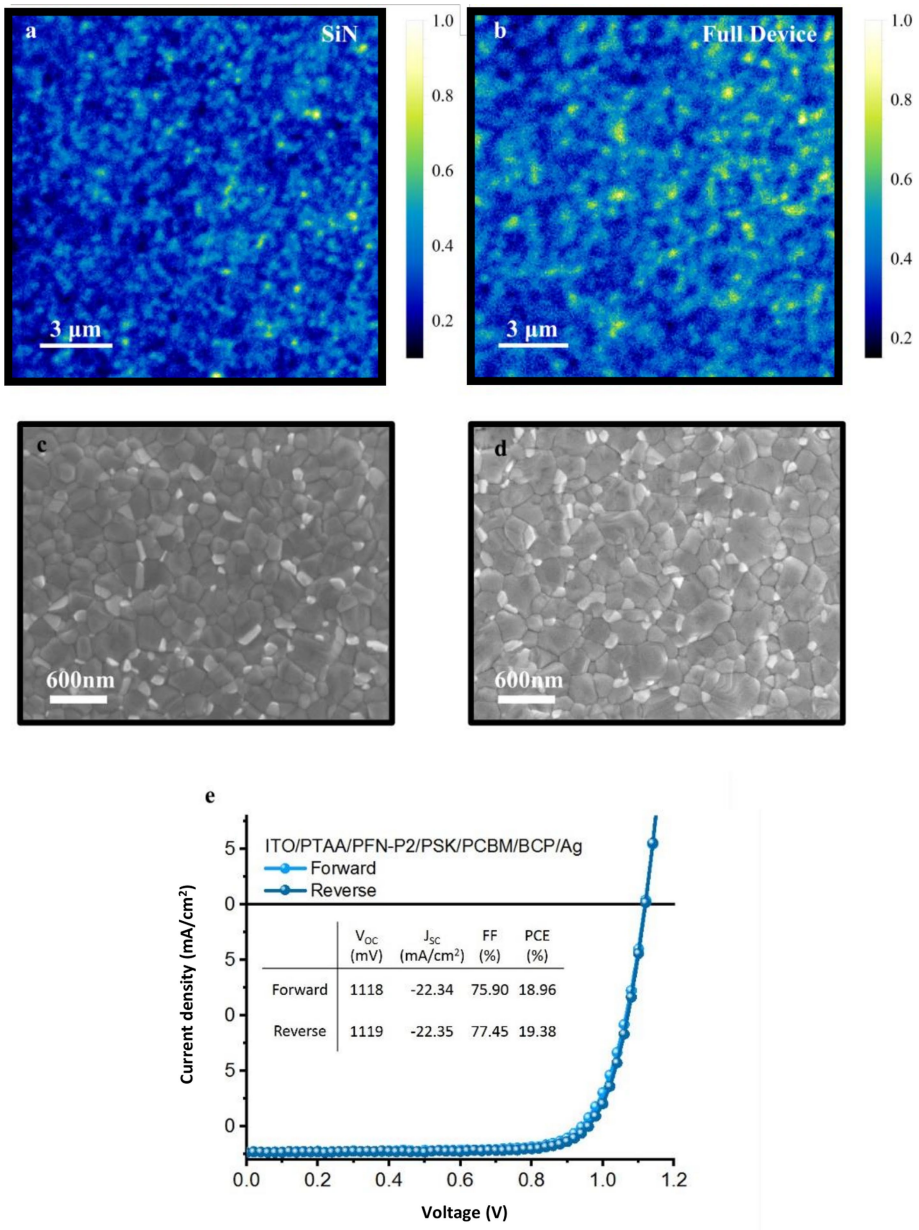

	V_{OC} (mV)	J_{SC} (mA/cm²)	FF (%)	PCE (%)
Forward	1118	-22.34	75.90	18.96
Reverse	1119	-22.35	77.45	19.38

Extended Data Fig. 2 | Normalized PL maps and key device performance metrics. PL maps were acquired using a pulsed 404-nm laser (repetition rate 2 MHz), focused through an objective lens (100× magnification, 0.9 NA) with an average power of 1.3 nW (~6 suns). **a**, PL map of a $(Cs_{0.05}FA_{0.78}MA_{0.17})Pb(I_{0.83}Br_{0.17})_3$ cation film deposited on a SiN window. **b**, PL map of a $(Cs_{0.05}FA_{0.78}MA_{0.17})Pb(I_{0.83}Br_{0.17})_3$ film in a full device stack (ITO/PTAA/PFN-P2/perovskite/PCBM/BCP/Ag). Both PL maps exhibit similar spatial variations in luminescent properties. **c**, Top-view SEM image of film deposited on SiN. **d**, Top-view SEM image of film deposited on ITO showing similar morphology and grain size to **c**. **e**, Performance metrics of a solar cell fabricated from the same material sample batch as **a**–**d**. FF, fill factor; J_{sc}, short-circuit current density; PCE, power conversion efficiency; PSK, perovskite; V_{oc}, open-circuit voltage.

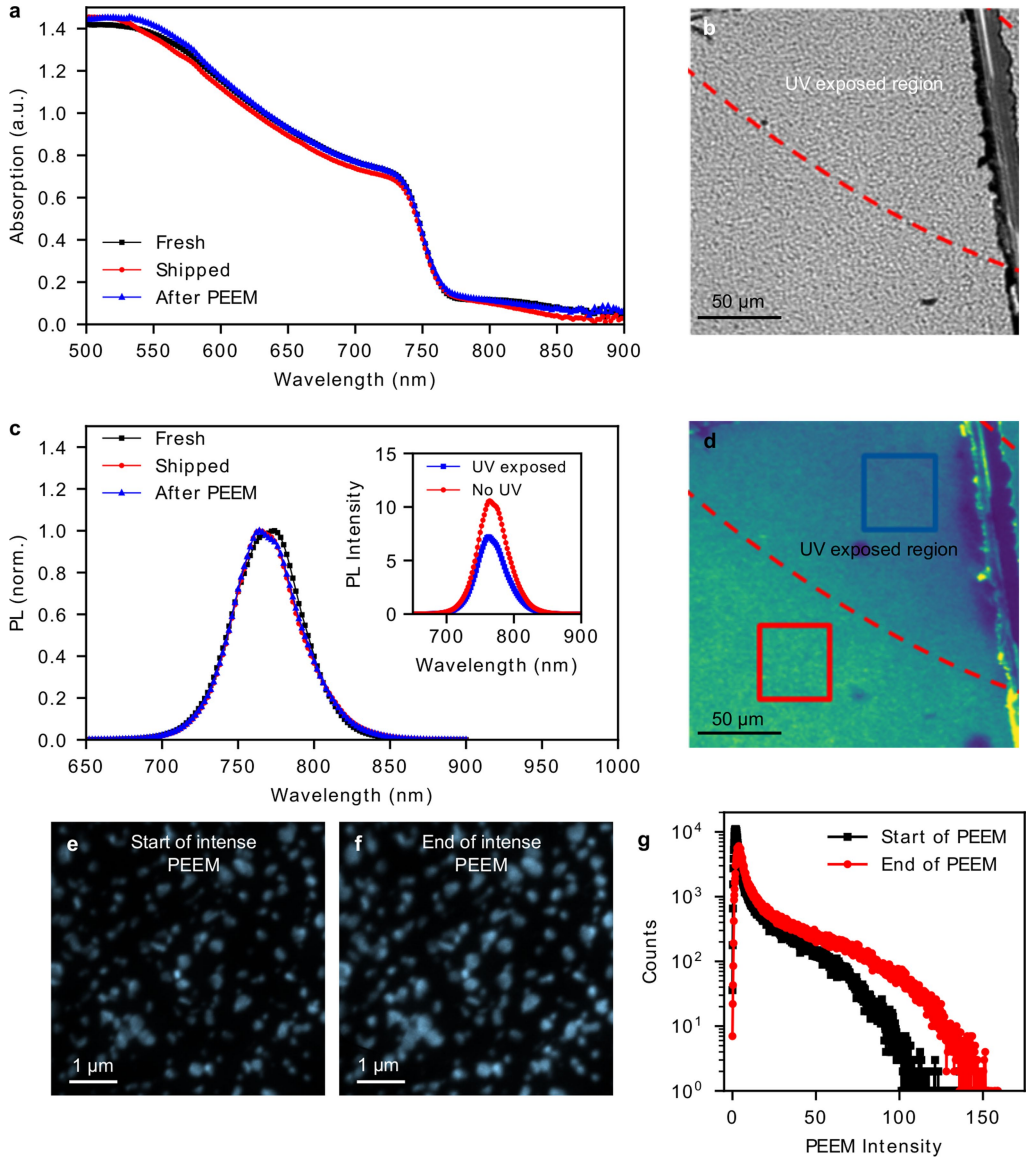

Extended Data Fig. 3 | Control experiments for PEEM measurements under strong and extended UV exposure (~7 h of 100 nJ cm^{-2} per pulse, ~10 kJ cm^{-2} total dose) on ($Cs_{0.05}FA_{0.78}MA_{0.17}$)$Pb(I_{0.83}Br_{0.17})_3$ samples. a, Optical absorption on freshly made samples (black squares), samples shipped under N_2 (red dots) and shipped samples after extensive UV exposure in PEEM (blue triangles). **b**, Optical reflectivity image of an area partially exposed to UV in PEEM (red dashed oval, partly shown). **c**, Normalized PL emission of fresh, shipped and UV-exposed samples. Inset, PL intensity from unexposed (red dots) and UV-exposed (blue squares). **d**, PL map of the location in **b**, showing a slight reduction in PL intensity in the UV-exposed region. **e**, **f**, PEEM images of the traps (4.65-eV probe) at the beginning (**e**) and end (**f**) of the 7-h UV exposure. **g**, Intensity histograms for the images in **e** and **f**.

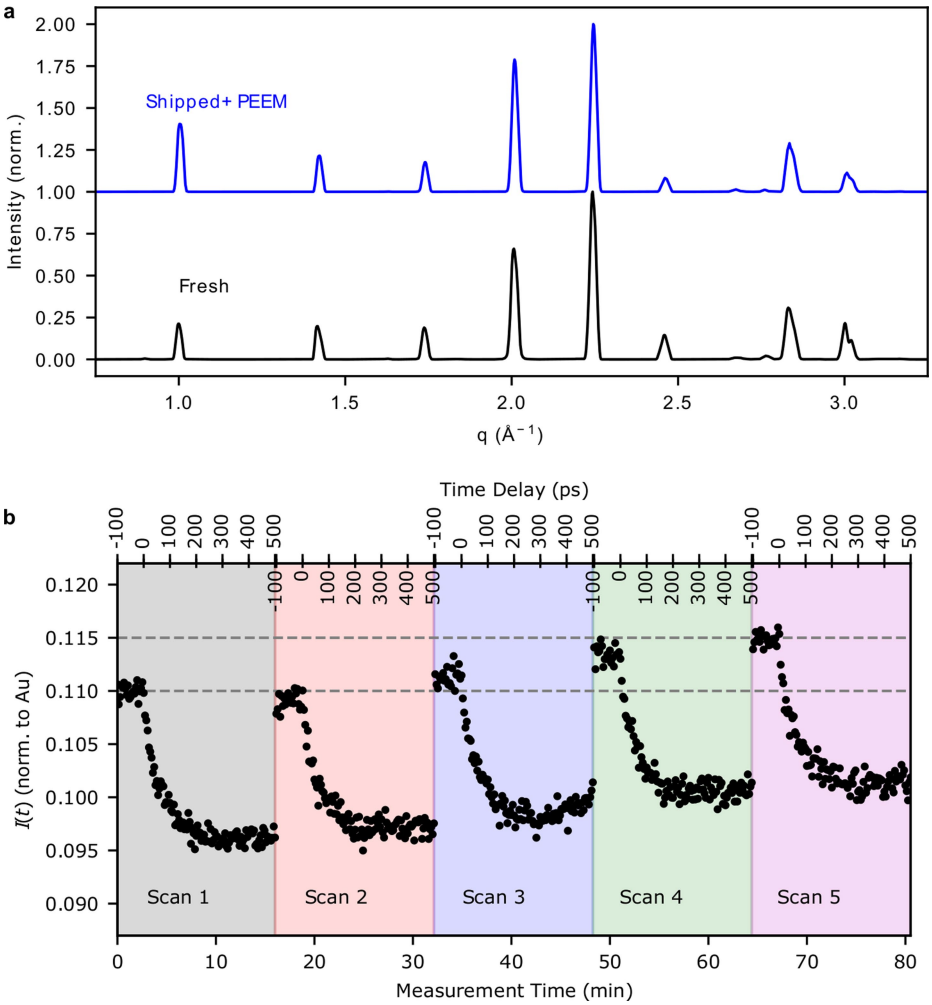

Extended Data Fig. 4 | Control measurements under normal measurement conditions. a, XRD measurements averaged over ~30 × 30 μm^2 on freshly made $(Cs_{0.05}FA_{0.78}MA_{0.17})Pb(I_{0.83}Br_{0.17})_3$ samples (black line) and samples after shipping and PEEM imaging (blue line). **b**, Five repeated TR-PEEM measurements (1.55-eV pump, 4.65-eV probe) on a $(Cs_{0.05}FA_{0.78}MA_{0.17})PbI_3$ sample taken in sequence and the corresponding real time of exposure shown on the bottom *x*-axis. The signal is averaged over the 10-μm FOV. We see an increase of ~4% in the trap density (for example, the flat plateaus at negative time delays, represented by the dashed grey lines) over the 80 min of measurement time.

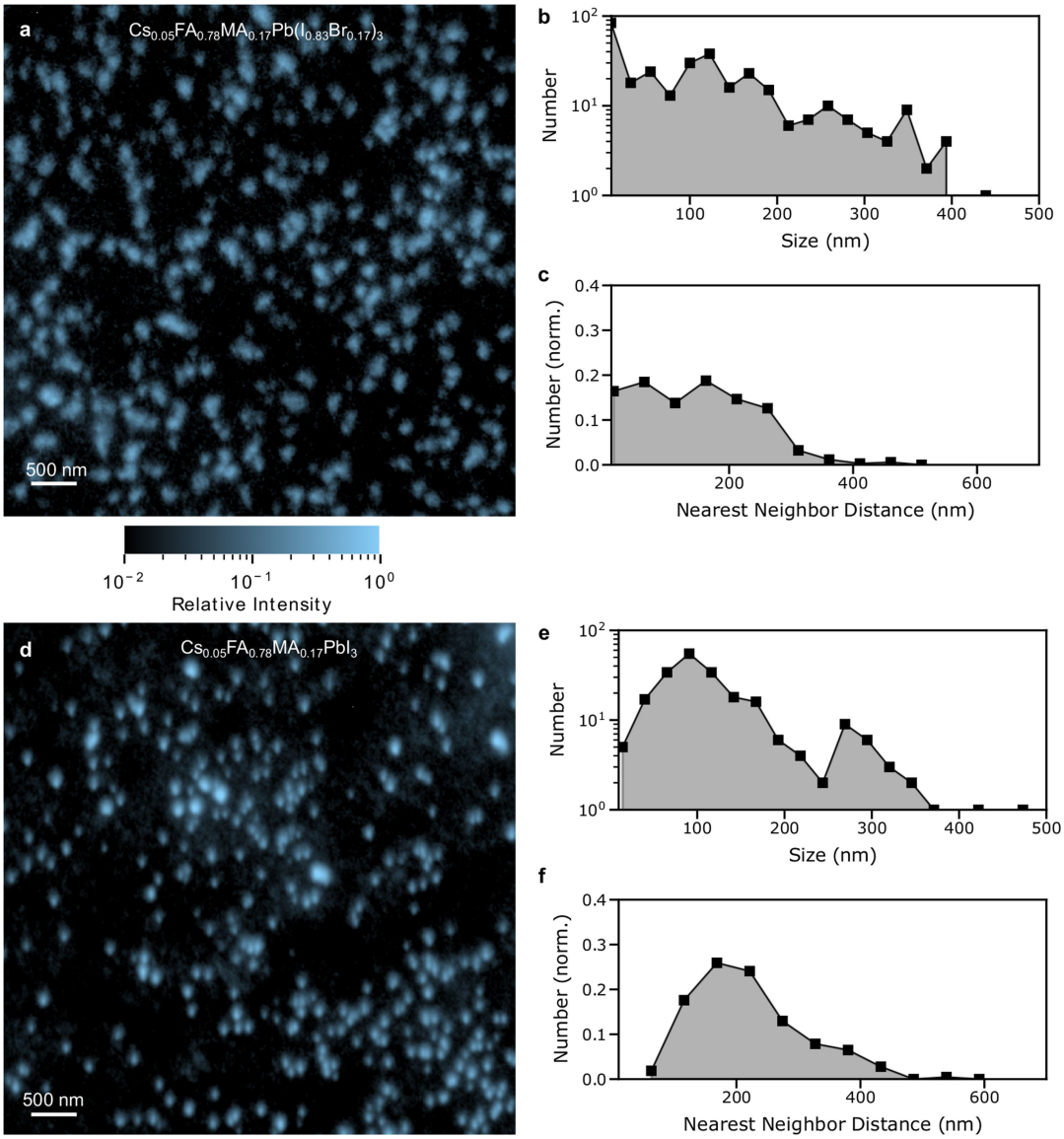

Extended Data Fig. 5 | Trap size and distance distributions. a, Normalized PEEM image of the traps for the $Cs_{0.05}FA_{0.78}MA_{0.17}Pb(I_{0.83}Br_{0.17})_3$ sample. **b**, Size distribution of the traps in image **a**. **c**, The distribution of distances between nearest neighbouring traps in **a**, resulting in a mean neighbour distance of 166 ± 95 nm (± standard deviation). **d**, Normalized PEEM image of traps in the $Cs_{0.05}FA_{0.78}MA_{0.17}PbI_3$ sample. **e**, Size distribution of the traps in image **d**. **f**, The distribution of distances between nearest neighbouring traps in **d**, resulting in a mean neighbour distance of 250 ± 90 nm (± standard deviation). Note that images **a** and **d** are on a logarithmic intensity scale.

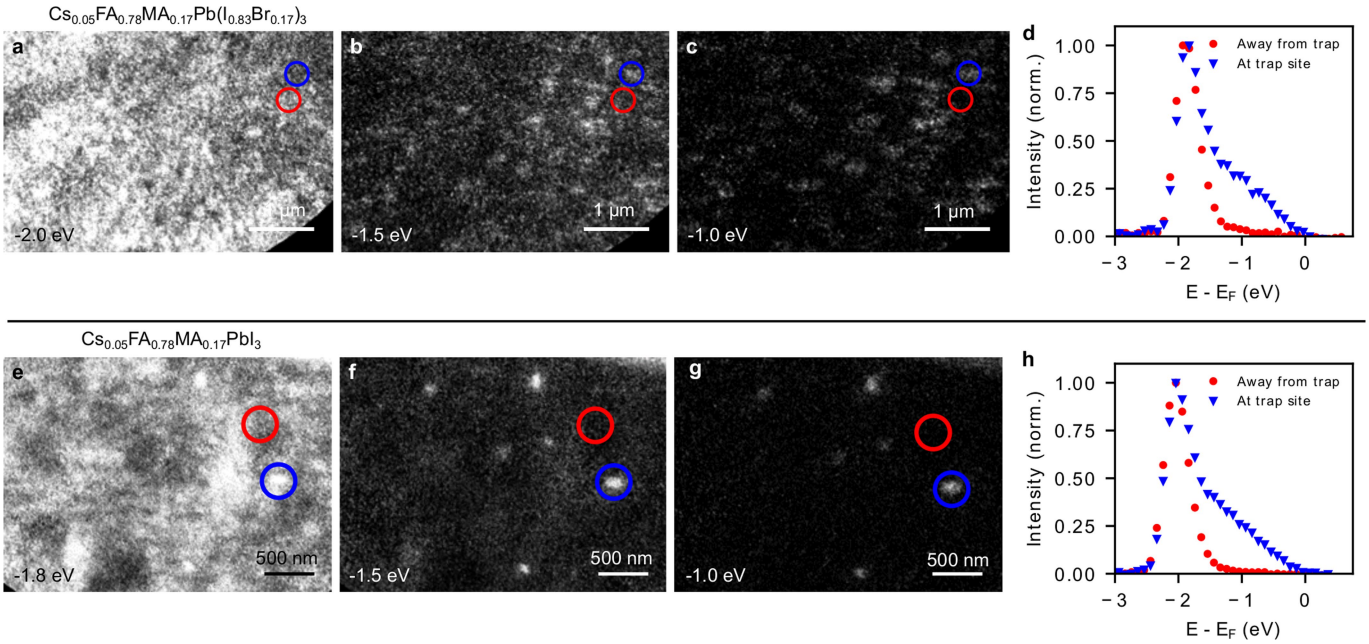

Extended Data Fig. 6 | Energy-resolved PEEM images and selected-area photoemission spectra. a–**c**, Energy-resolved PEEM images of $Cs_{0.05}FA_{0.78}MA_{0.17}Pb(I_{0.83}Br_{0.17})_3$ at $E - E_F = -2.0$ eV, −1.5 eV and −1.0 eV, respectively. **d**, The extracted photoemission spectra from the regions circled in red (away from a trap) and blue (at trap sites) in **a**–**c**. **e**–**g**, Energy-resolved PEEM images of a $Cs_{0.05}FA_{0.78}MA_{0.17}PbI_3$ sample at $E - E_F = -1.8$ eV, −1.5 eV and −1.0 eV, respectively. **h**, The extracted photoemission spectra from the blue and red circled regions shown in **e**–**g**.

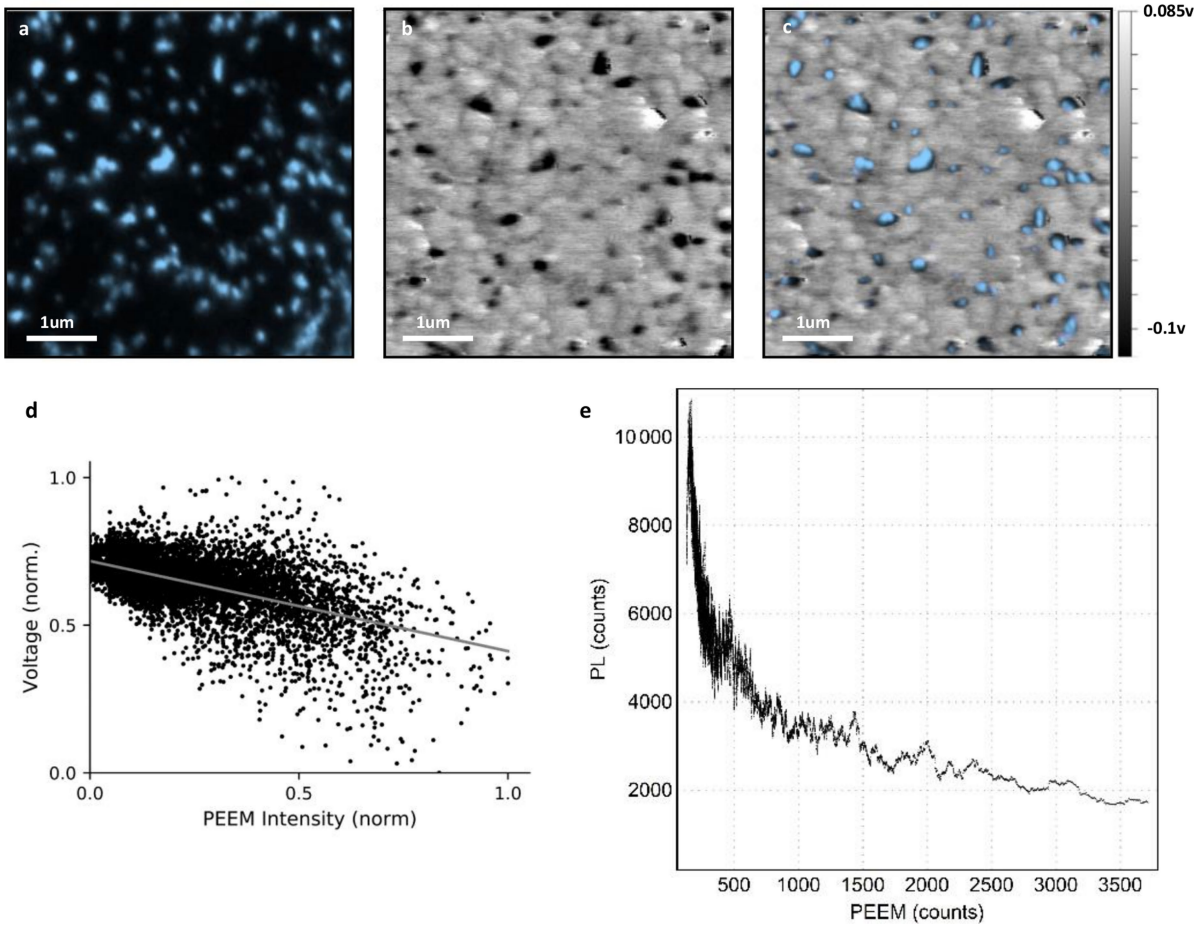

Extended Data Fig. 7 | KPFM–PEEM intensity correlation and PL–PEEM intensity correlation. a, PEEM map of a $Cs_{0.05}FA_{0.78}MA_{0.17}Pb(I_{0.83}Br_{0.17})_3$ film. **b**, KPFM map of the same region as **a**, revealing dark regions with CPD deviating from the surrounding bulk. **c**, Overlay of PEEM (blue) and KPFM (grey), illustrating the strong correlation between the location of the PEEM spots and the KPFM features. **d**, Statistically significant negative correlation between the CPD and the PEEM intensity (Pearson's correlation coefficient −0.58, *P*-value <0.001). The difference in CPD observed between the regions at a trap site, and away from a trap site, is similar to the energy resolution of our PEEM set-up (~150–200 meV). **e**, PL–PEEM pixel-by-pixel moving average intensity correlation of Fig. 1c. This reproduces the correlation behaviour seen spatially, where high-intensity PL only occurs at pixels with low PEEM intensity, and high-intensity PEEM pixels only show low PL intensity.

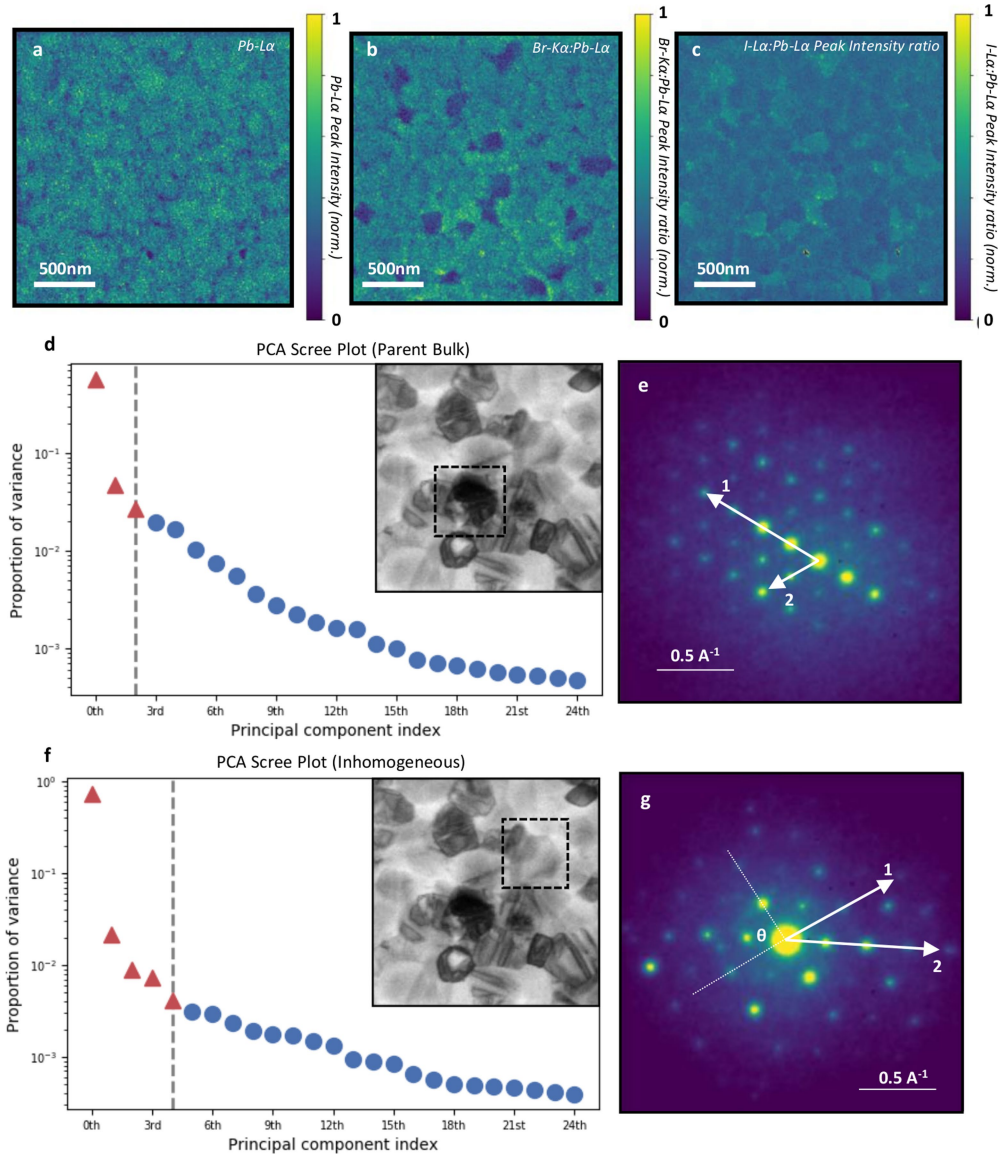

Extended Data Fig. 8 | Extended structural and compositional characterization of a $Cs_{0.05}FA_{0.78}MA_{0.17}Pb(I_{0.83}Br_{0.17})_3$ thin film. a, Pb Lα peak intensity map obtained from STEM-EDX measurements. **b**, Peak intensity map of the ratio Br Kα:Pb Lα for the same region as **a**. **c**, Peak intensity map of the ratio I Lα:Pb Lα. All maps are normalized between 0 and 1 by dividing by the maximum value extracted from the respective maps of peak intensity ratio. **d**, PCA scree plot of the parent bulk region indicated in inset to **d**. Components are plotted in order of decreasing variance and the knee point is illustrated by a vertical line. Red triangles represent high-variance components, blue circles low-variance components. **e**, Mean diffraction pattern extracted from the grain in Fig. 3c revealed by the three-factor non-negative matrix factorization (NMF) of the region indicated in **d** inset. Vector lengths marked 1 and 2 are 0.889 A^{-1} and 0.456 A^{-1} respectively. These lengths compare closely to the predicted lengths of the $(40\bar{4})$ reflection (0.898 A^{-1}) and the $(02\bar{2})$ reflection (0.449 A^{-1}) in cubic $FAPb(I_{0.83},Br_{0.17})_3$. The calculated angle between 1 and 2 is 60.6°. The predicted angle between the $(40\bar{4})$ and $(02\bar{2})$reflections in cubic $FAPb(I_{0.83},Br_{0.17})_3$ is 60°. Together, these results index the diffraction pattern (Fig. 3c and Extended Data Fig. 8e) of the grain shown in Fig. 3a–d to be near the [111] zone axis of a cubic $FAPb(I_{0.83},Br_{0.17})_3$ structure. **f**, PCA scree plot of the compositionally inhomogeneous region indicated in **f** inset. Components are plotted in order of decreasing variance, and the knee point is illustrated by a vertical line. Red triangles represent high-variance components, blue circles low-variance components. **g**, Mean diffraction pattern extracted from the grain in Fig. 3g by the five-factor NMF of the region indicated in f – inset. The diffraction pattern cannot be definitively indexed to either a perovskite or PbI_2 structural model.

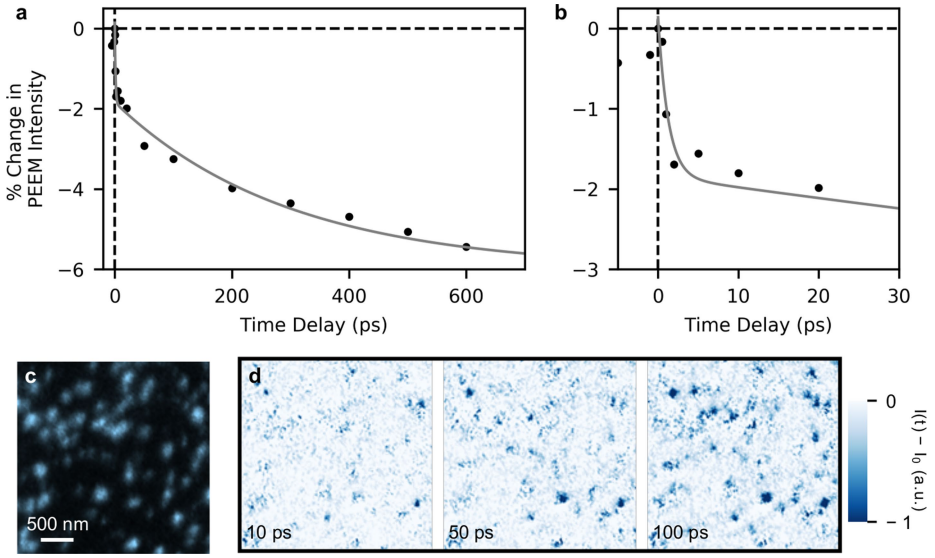

Extended Data Fig. 9 | TR-PEEM data from a $Cs_{0.05}FA_{0.78}MA_{0.17}Pb(I_{0.83}Br_{0.17})_3$ thin film sample. a, Percentage change in the PEEM intensity (4.65-eV probe) after pump excitation (1.55 eV), averaged over all trap sites in the ~10 × 10 μm^2 field of view. Here, the pump fluence is ~100 μJ cm^{-2} per pulse, due to the low absorption at this photon energy. The grey line is a fit to a double exponential, yielding the amplitudes and time constants $A_1 = 2.0 \pm 0.3$, $A_2 = 4.2 \pm 0.4$, $\tau_1 = 1.3 \pm 0.5$ ps and $\tau_2 = 300 \pm 80$ ps, where the error is the standard error of the fit. **b**, Zoom-in of the signal at shorter time delays, where the fast component of the signal can be more easily seen. **c**, PEEM image of a cluster of trap sites. **d**, TR-PEEM difference images of **c** at several pump-probe time delays.

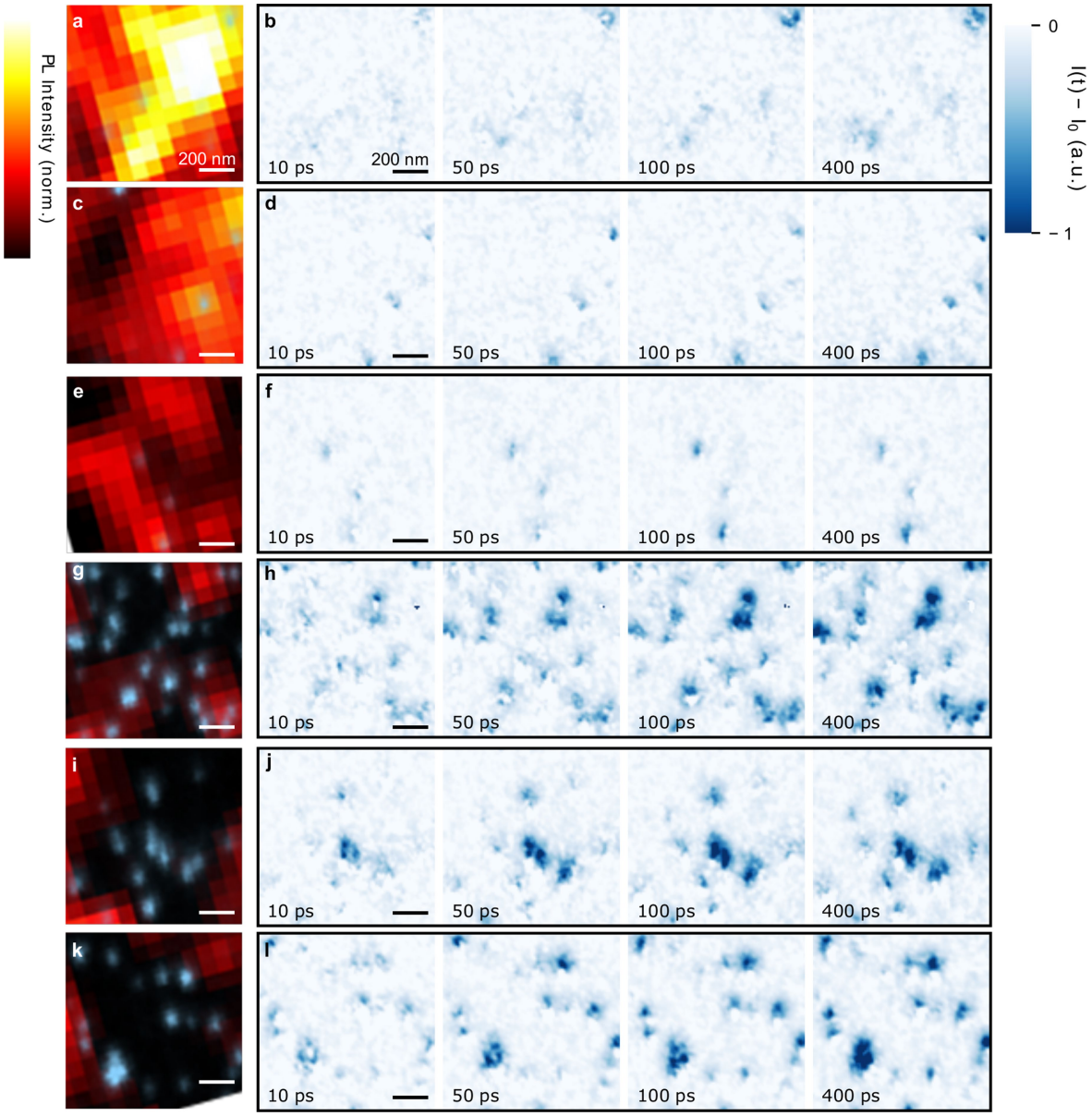

Extended Data Fig. 10 | Additional selected PL–PEEM overlays and TR-PEEM images for the $Cs_{0.05}FA_{0.78}MA_{0.17}PbI_3$ sample. a, **c**, **e**, **g**, **i**, **k**, PL–PEEM overlays of selected regions of higher (**a**–**e**) and lower (**g**–**k**) PL yield. **b**, **d**, **f**, **h**, **j**, **l**, TR-PEEM difference images for the same locations at several time delays.

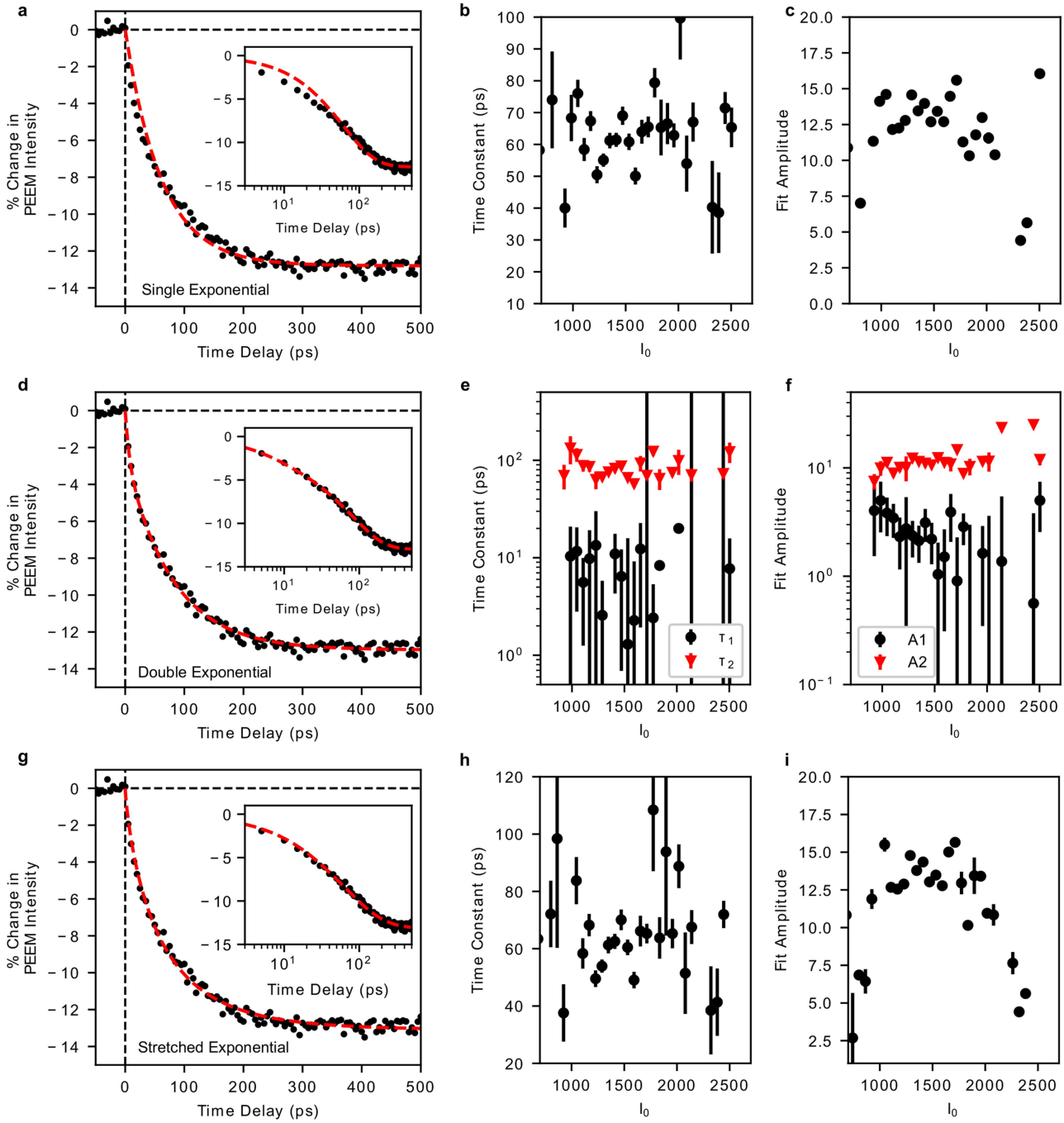

Extended Data Fig. 11. | Comparison of different fitting functions for analysing trapping kinetics in a $Cs_{0.05}FA_{0.78}MA_{0.17})PbI_3$ thin film. **a**, Single-exponential fit (red dashed line) to the integrated TR-PEEM data, with log-scale inset. **b**, **c**, The corresponding single-exponential time constants (**b**) and amplitudes (**c**) as a function of the bin intensity I_0. **d**, Double-exponential fit to the data (same as shown in Fig. 4c), with log-scale inset. **e**, **f**, The corresponding time constants (**e**) and amplitudes (**f**) for the double-exponential fit as a function of the bin intensity. **g**, Stretched exponential fit to the TR-PEEM data, with log-scale inset. **h**, **i**, The corresponding time constants (**h**) and amplitudes (**i**) for the stretched exponential fit as a function of bin intensity. For all fit parameters, the error bars represent the standard error from fitting for each intensity bin, where the number of traps measured for each bin is shown by the histogram in Extended Data Fig. 12b. Empty bins or bins with no signal (that is, fit routine fails) are excluded.

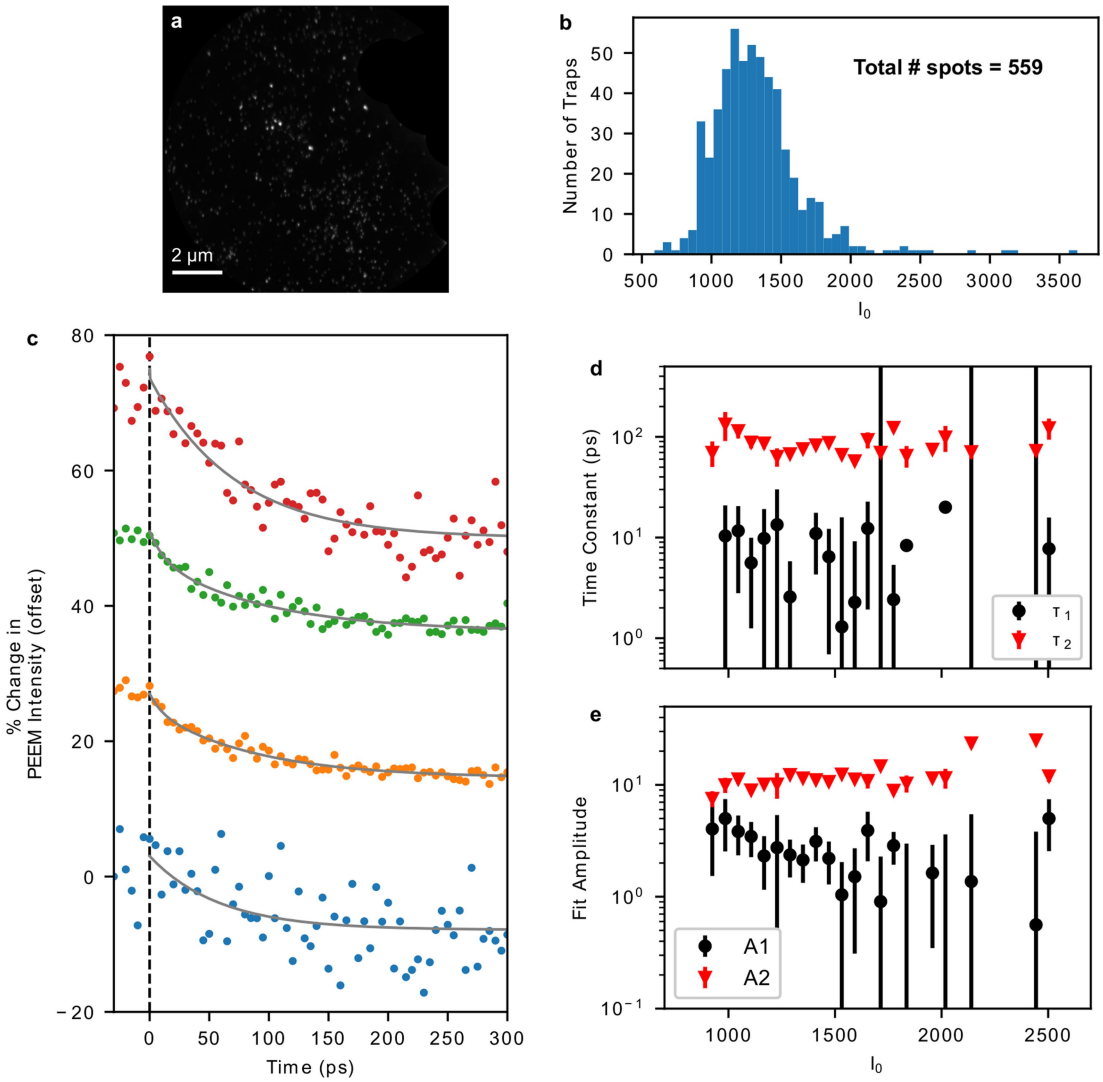

Extended Data Fig. 12 | Intensity bin analysis of trapping dynamics in a ($Cs_{0.05}FA_{0.78}MA_{0.17}$)$PbI_3$ thin film. a, PEEM image of traps, with the Au marker masked out. **b**, Intensity histogram of the spots identified in **a** for 50 equally spaced intensity bins. **c**, TR-PEEM dynamics (spots) and double-exponential fits (grey lines) for four of the intensity bins in **b**. **d**, **e**, Fitted time constants (**d**) and amplitudes (**e**) as a function of the binned trap intensity (I_0), where the number of traps in each intensity bin is shown by the histogram in **b**.